Differential Framework for Submeter-Accurate Vehicular Navigation With Cellular Signals

Joe Khalife, *Member, IEEE*, and Zaher M. Kassas, *Senior Member, IEEE*

***Abstract*—A framework that could achieve submeter-level-accurate horizontal navigation with carrier phase differential measurements from cellular signals is developed. This framework, termed CD-cellular, is composed of a base and a rover in a cellular environment, both making carrier phase measurements to the same cellular base transceiver stations (BTSs). The base shares its carrier phase measurements with the mobile rover, which in turn employs an extended Kalman filter to obtain a coarse estimate of its states, followed by a batch weighted nonlinear least squares (B-WNLS) estimator to solve for the integer ambiguities, and finally a point-solution WNLS to estimate its own states. The framework is designed to guarantee that after some time, the rover's position error remains below a pre-defined threshold with a desired probability. This is achieved by leveraging models of the BTS positions from stochastic geometry. Experimental results on an unmanned aerial vehicle (UAV) in an open semi-urban environment with multipath-free, line-of-sight (LOS) conditions are presented, showing that the developed framework achieves a 70.48 cm position root mean-squared error (RMSE) over a trajectory of 2.24 km, measured with respect to the UAV's navigation solution from its onboard GPS-inertial navigation system (INS).**

***Index Terms*—Carrier phase, fifth-generation (5G), integer ambiguity resolution, LTE, navigation, RTK, signals of opportunity, UAV.**

NOMENCLATURE

i	$\in \{\text{UAV(U)}, \text{Base(B)}\}$, receiver index.
n	$\in \{1, \ldots, N\}$, BTS index.
N	Total number of BTSs.
k	Discrete-time index.
c	Speed of light.
λ	Signal wavelength.
$z_n^{(i)}(k)$	Carrier phase measurement from i-th receiver to n-th BTS at time-step k.
$\boldsymbol{r}_{r_i}$	$\triangleq [x_{r_i}, y_{r_i}]^\mathsf{T}$, i-th receiver's two-dimensional (2-D) position vector.
$\boldsymbol{r}_{s_n}$	$\triangleq [x_{s_n}, y_{s_n}]^\mathsf{T}$, n-th BTS's 2-D position vector.
$\Delta z_{r_i,s_n}$	Altitude difference between i-th receiver and n-th BTS.
$N_n^{(i)}$	Carrier phase ambiguity between i-th receiver and n-th BTS.
δt_{r_i}	i-th receiver's clock bias.
δt_{s_n}	n-th BTS's clock bias.
$v_n^{(i)}$	Measurement noise between i-th receiver and n-th BTS.
$(\sigma_n^{(i)})^2$	Variance of $v_n^{(i)}$.
$C/N_{0,n}^{(i)}$	Carrier-to-noise ratio of n-th BTS measured by i-th receiver.
$B_{i,\text{PLL}}$	i-th receiver's PLL noise equivalent bandwidth.
$z_{n,1}^{(\text{U,B})}$	Double-difference carrier phase measurment for n-th BTS.
$h_{n,1}^{\text{U}}$	Single-difference range for n-th BTS.
$N_{n,1}^{(\text{U,B})}$	Double-difference integer ambiguity for n-th BTS.
$v_{n,1}^{(\text{U,B})}$	Double-difference measurement noise for n-th BTS.
$\boldsymbol{z}_{\text{U,B}}$	Vector of all double-difference measurements.
$\boldsymbol{h}[\boldsymbol{r}_{r_\text{U}}]$	Vector of all single-difference ranges.
$\boldsymbol{N}$	Vector of all double-difference integer ambiguities.
$\boldsymbol{v}_{\text{U,B}}$	Vector of all double-difference measurement noise.
$\mathbf{R}_{\text{U,B}}$	Covariance matrix of $\boldsymbol{v}_{\text{U,B}}$.
α	Confidence level.
ζ	Desired position error threshold.
k_ζ	Cutoff time beyond which position error bound holds.
$\mathbf{z}_{\text{U,B}}^{k_\zeta}$	Collection of all double-difference measurement vectors up to time-step k_ζ.
$\mathbf{r}_{\boldsymbol{r}_\text{U}}^{k_\zeta}$	Time history of receiver U's position up to time-step k_ζ in vector form.
$\mathbf{h}[\mathbf{r}_{\boldsymbol{r}_\text{U}}^{k_\zeta}]$	Collection of all single-difference range vectors up to time-step k_ζ.
$\mathbf{v}_{\text{U,B}}^{k_\zeta}$	Collection of all double-difference measurement noise vectors up to time-step k_ζ.
$\mathbf{R}_{\text{U,B}}^{k_\zeta}$	Covariance matrix of $\mathbf{v}_{\text{U,B}}^{k_\zeta}$.
$\hat{\mathbf{r}}_{\boldsymbol{r}_\text{U}}^{k_\zeta}$	B-WNLS float estimate of $\hat{\mathbf{r}}_{\boldsymbol{r}_\text{U}}^{k_\zeta}$.
$\hat{\boldsymbol{N}}^{k_\zeta}$	B-WNLS float estimate of $\boldsymbol{N}$.
$\check{\boldsymbol{N}}^{k_\zeta}$	B-WNLS integer estimate of $\boldsymbol{N}$.
$\tilde{\boldsymbol{N}}^{k_\zeta}$	Integer ambiguity errors.
$\check{\mathbf{r}}_{\boldsymbol{r}_\text{U}}^{k_\zeta}$	B-WNLS estimate of $\hat{\mathbf{r}}_{\boldsymbol{r}_\text{U}}^{k_\zeta}$ after integer fix.
$\tilde{\mathbf{G}}$	Double-difference geometry matrix.

Manuscript received 6 June 2022; accepted 18 June 2022. Date of publication 1 August 2022; date of current version 23 January 2023. This work was supported in part by the Office of Naval Research under Grant N00014-19-1-2511, in part by the National Science Foundation under Grant 1929965, and in part by the U.S. Department of Transportation under Grant 69A3552047138 for the CARMEN University Transportation Center. (*Corresponding author: Zaher M. Kassas.*)

Joe Khalife is with the Department of Mechanical and Aerospace Engineering, University of California, Irvine, CA 92697 USA (e-mail: khalifej@uci.edu).

Zaher M. Kassas is with the Department of Electrical and Computer Engineering, the Ohio State University, Columbus, OH 43210 USA (e-mail: zkassas@ieee.org).

Color versions of one or more figures in this article are available at https://doi.org/10.1109/TIV.2022.3187957.

Digital Object Identifier 10.1109/TIV.2022.3187957

$\lambda_{\max}(\mathbf{A})$ Maximum eigenvalue of some matrix $\mathbf{A}$.
$\lambda_{\min}(\mathbf{A})$ Minimum eigenvalue of some matrix $\mathbf{A}$.
$f^{-1}_{\chi^2,M}(\cdot)$ Inverse chi-square cdf with M degrees of freedom.

I. Introduction

As AUTONOMOUS vehicles (AVs) get endowed with higher levels of autonomy, the accuracy and resiliency requirements of their navigation systems become evermore stringent. For example, for an automated driving system to be classified as SAE J3016™ Level 4 (high automation), the driving system must be able to precisely and safely execute driving maneuvers, such as lane changes or turns at intersections. In order to execute such driving maneuvers, localization accuracies of 0.1 m with a confidence of 95% must be realized [1]. On the other hand, while similar clear-cut requirements for unmanned aerial vehicles (UAVs) have not been established yet [2], [3], it is not far-fetched to imagine submeter-level navigation requirements for certain flight operations, e.g., beyond visual line-of-sight (BVLOS) in urban environments and in large-scale swarms.

Today's AVs rely on an inertial navigation system (INS) aided by global navigation satellite system (GNSS) signals. While such systems can meet the submeter-level accuracy requirement in certain clear line-of-sight conditions, they are at the mercy of GNSS signal vulnerabilities. These signals are jammable, spoofable, and may become unusable in certain environments (e.g., deep urban canyons) [4]–[7]. Moreover, a GNSS receiver may simply fail altogether. When GNSS signals are compromised or unusable, the error in the INS-derived navigation solution will quickly drift unboundedly, violating the navigation accuracy requirement and jeopardizing the safe operation of the AV. On one hand, aiding sensors such as lidars or cameras can be used to limit the drift of the INS [8], [9]. However, such sensors can only provide position information in a *local* map and they too could drift over time [10], [11]. One way to circumvent this issue is to create high-fidelity global maps of lidar point clouds or camera images and localize the AV in such global maps using map matching [12]. However, building these high-fidelity maps for different environment is tedious and performing map matching requires high computational power and resources to run in real-time [13], [14]. On the other hand, signals of opportunity (SOPs) (e.g., low Earth orbit (LEO) satellite [15]–[17], digital television [18], [19], and cellular [20]–[26]) possess desirable attributes to serve as an alternative aiding source to GNSS signals. Navigation with SOPs has been demonstrated on ground vehicles and unmanned aerial vehicles (UAVs), achieving a localization accuracy ranging from meters to tens of meters, with the latter accuracy corresponding to ground vehicles in deep urban canyons with severe multipath conditions [27]–[33]. Cellular SOPs, particularly 3G code-division multiple access (CDMA), 4G long-term evolution (LTE), and 5G new radio (NR), are among the most attractive SOP candidates for navigation. These signals are abundant, received at a much higher power than GNSS signals, offer a favorable horizontal geometry, are free to use, and can provide position information in a *global* map. While cellular signals are jammable and spoofable [34]–[36], they are typically received at high powers (more than 30 dB than GNSS signals [37]) and are transmitted in multiple frequency bands. The cellular 3G, 4G, and 5G spectrum spans the 700 MHz to nearly 6 GHz bands. The 5G millimeter wave (mmWave) spectrum is envisioned to span several GHz of spectrum, with some bands reaching up to 400 MHz of bandwidth. This makes staging a successful, clandestine attack on cellular SOPs generally challenging, as the attacker would need to target the entire cellular spectrum with very high power.

A challenge that arises in cellular-based navigation is the unknown states of cellular base transceiver stations (BTSs), namely their position and clock errors (bias and drift). This is in sharp contrast to GNSS-based navigation, where the states of the satellites are transmitted to the receiver in the navigation message. Since cellular BTSs are spatially stationary, their positions may be mapped prior to navigation (e.g., by a dedicated mapping campaign or from satellite imagery and cellular databases). While mapping BTS positions is also tedious, the number of BTSs in an environment is orders of magnitude lower than the number of points in a lidar point cloud or pixels in image maps. While BTS positions can be mapped once and stored for later use, BTS clock errors must be continuously estimated since these errors are stochastic and dynamic. To deal with this challenge, a base/rover framework was proposed in [20], [38], in which the base and rover make pseudorange measurements to the same BTSs in the environment. The base was assumed to have complete knowledge of its states (e.g., by having access to GNSS signals), while estimating the states of BTSs in its environment, and sharing these estimates with a rover that had no knowledge of its states. Another framework was developed in which the rover estimated its states simultaneously with the states of the BTSs in the environment, i.e., performed radio simultaneous localization and mapping (radio SLAM) [39], [40].

It is well-known that carrier phase measurements are much more precise than code phase (pseudorange) measurements. While meter-level accuracy is achievable with pseudorange measurements, submeter-level (centimeter to decimeter) is achievable in carrier phase differential GNSS (CD-GNSS), also known as real-time kinematic (RTK) [41], [42]. However, the literature on differential cellular-based navigation frameworks is sparse. A preliminary study of cellular carrier phase-based navigation were conducted in [43], [44], in which the received carrier phase of cellular signals was exploited to produce submeter-level accurate navigation solutions on a UAV flying in an open semi-urban environment. The framework was based on carrier phase differential (CD)-cellular measurements, requiring an additional base receiver. The CD-cellular navigation framework was analyzed through Monte Carlo simulations. One advantage of the CD-cellular framework is that it requires very few base receivers to cover large areas [44] (1 base in about 6 km radius). One challenge with using differential carrier phase measurements is having to resolve the integer ambiguities [41], [45], [46]. Several solutions have been proposed for this problem, most notably the Local Minima Search (LMS) method [47] and the Least-squares Ambiguity Decorrelation Adjustment (LAMBDA) method [48]–[50] and its variants [51]. These methods rely on either (i) multiple-frequency measurements, both code and carrier phase measurements, (ii) the GNSS satellite geometry to change significantly

with time as the receiver remains stationary, or (iii) dedicated ground-based GPS integrity beacons [52]. However, code phase measurements are not necessarily available from cellular BTSs, nor do BTSs necessarily transmit synchronized signals on different frequencies; and BTSs are stationary. To overcome this issue, a CD-cellular framework that leverages UAV motion to resolve the integer ambiguities and achieve a submeter-accurate navigation solution was proposed in [44]. However, the work in [44] suffers from two major limitations: (i) the navigation solution prior to resolving the ambiguities lacks rigorous reliability guarantees and (ii) the size of the batch filter that resolves the ambiguities is pre-set, which does not guarantee any navigation performance requirements.

This paper presents the first complete study for submeter-accurate horizontal navigation using CD-cellular measurements. The framework requires a base receiver making carrier phase measurements to the same BTSs as the navigating rover and assumes a communication channel between the base and rover. While this framework could be employed for ground or aerial vehicles (as long as multipath and signal blockage conditions are properly mitigated or accounted for), this study focuses on UAV applications, due to the favorable multipath-free, line-of-sight (LOS) channels between the BTS and the UAV. It is important to note that the algorithms presented in the paper are agnostic to the signal type. The CD-cellular framework only assumes carrier phase measurements available from nearby cellular towers, which can be produced from 3G, 4G, 5G, and future generations. In particular, this paper extends [43] and [44] by making the following four contributions:

1) First, a three-stage framework for navigating with CD-cellular measurements is developed. The first stage employs an extended Kalman filter (EKF) to obtain a coarse estimate of the UAV's position. An EKF initialization scheme is provided. In the second stage, a batch solution is obtained to fix the integer ambiguities. In the third stage, the UAV navigates with the CD-cellular measurements and fixed ambiguities.
2) A probabilistic upper bound on the position error after resolving the integer ambiguities is established. The probabilistic upper bound captures mainly the effect of the integer ambiguity error on the UAV position error. Models of the BTS positions from stochastic geometry are leveraged to determine the upper bound that holds with a desired probability, for a given number of BTSs.
3) The derived probabilistic upper bound is used to formulate a test that determines when to solve the batch estimator and fix the integer ambiguities in order to guarantee that the UAV position error remains under a pre-defined threshold, with a certain probability.
4) Experimental results are presented demonstrating the proposed CD-cellular framework. The experiments show a UAV navigating at submeter-level accuracy in an open semi-urban environment and multipath-free, LOS conditions, while remaining in the same BTS sectors. The UAV achieves a horizontal position root mean-squared error (RMSE) of 70.48 cm over a trajectory of 2.24 km, measured with respect to the UAV's navigation solution from its onboard GPS-INS.

The remainder of the paper is organized as follows. Section II describes the cellular carrier phase observable model. Section III formulats the base/rover CD-cellular framework. Section IV provides experimental results demonstrating the proposed framework, showing submeter-level UAV navigation accuracy. Concluding remarks are given in Section V.

II. Cellular Carrier Phase Observable Model

In the rest of this paper, availability of code phase, Doppler frequency, and carrier phase measurements of cellular CDMA and LTE signals is assumed (e.g., from specialized navigation receivers [18], [20], [53]–[56]). The continuous-time carrier phase observable can be obtained by integrating the Doppler measurement over time [41]. The carrier phase (expressed in cycles) made by the i-th receiver on the n-th SOP is given by

$$\phi_n^{(i)}(t) = \phi_n^{(i)}(t_0) + \int_{t_0}^{t} f_{D_n}^{(i)}(\tau)d\tau, \quad n = 1, \ldots, N, \tag{1}$$

where $f_{D_n}^{(i)}$ is the Doppler measurement made by the i-th receiver on the n-th cellular SOP, $\phi_n^{(i)}(t_0)$ is the initial carrier phase, and N is the total number of SOPs. In (1), i denotes either the base (B) or the rover UAV (U). Assuming a constant Doppler during a subaccumulation period T, (1) can be discretized to yield

$$\phi_n^{(i)}(t_k) = \phi_n^{(i)}(t_0) + \sum_{l=0}^{k-1} f_{D_n}^{(i)}(t_l)T, \tag{2}$$

where $t_k \triangleq t_0 + kT$. In what follows, the time argument t_k will be replaced by k for simplicity of notation. Note that the receiver will make noisy carrier phase measurements. Adding measurement noise to (2) and expressing the carrier phase observable in meters yields

$$z_n^{(i)}(k) = \lambda\phi_n^{(i)} + \lambda T \sum_{l=0}^{k-1} f_{D_n}^{(i)}(l) + v_n^{(i)}(k), \tag{3}$$

where λ is the wavelength of the carrier signal and $v_n^{(i)}(k)$ is the measurement noise, which is modeled as a discrete-time zero-mean white Gaussian sequence with variance $[\sigma_n^{(i)}(k)]^2$. The carrier phase in (3) can be parameterized in terms of the receiver and cellular SOP states as

$$\begin{aligned} z_n^{(i)}(k) = {} & \sqrt{\|\boldsymbol{r}_{r_i}(k) - \boldsymbol{r}_{s_n}\|_2^2 + \Delta z_{r_i,s_n}^2(k)} \\ & + c\left[\delta t_{r_i}(k) - \delta t_{s_n}(k)\right] + \lambda N_n^{(i)} + v_n^{(i)}(k), \end{aligned} \tag{4}$$

where $\boldsymbol{r}_{r_i} \triangleq [x_{r_i}, y_{r_i}]^{\mathsf{T}}$ is the receiver's two-dimensional (2–D) position vector; $\boldsymbol{r}_{s_n} \triangleq [x_{s_n}, y_{s_n}]^{\mathsf{T}}$ is the cellular BTS's known 2–D position vector; $\Delta z_{r_i,s_n} \triangleq z_{r_i}(k) - z_{s_n}$ is the difference between the receiver' and BTS's altitude; c is the speed of light; δt_{r_i} and δt_{s_n} are the receiver's and cellular BTS's clock biases, respectively; and $N_n^{(i)}$ is the carrier phase ambiguity. Note that a coherent PLL may be employed in CDMA and LTE navigation receivers since the cellular synchronization and reference signals do not carry any data. As such, the measurement noise variance can be expressed as [41]

$$\left[\sigma_n^{(i)}(k)\right]^2 = \lambda^2 \frac{B_{i,\text{PLL}}}{C/N_{0,n}(k)}, \tag{5}$$

where $B_{i,\text{PLL}}$ is the receiver's PLL noise equivalent bandwidth and $C/N_{0,n}(k)$ is the cellular SOP's measured carrier-to-noise ratio at time-step k. The remainder of this paper assumes zero-mean Gaussian measurement noise. The actual measurement noise statistics may differ from the what is assumed in (5). Therefore, instead of using (5), Gaussian overbounds of the true measurement noise distribution could be used, if known. Methods described in [57]–[59] could be used to compute overbounds of the measurement noise statistics in different environments. Note that small UAVs and hearable cellular BTSs are typically at comparable altitudes, which makes the vertical diversity very poor. Therefore, one can only estimate the UAV's horizontal position using cellular SOPs without introducing significant errors. As such, the proposed framework assumes that the UAV and BTS altitudes, $z_r(k)$ and z_{s_n}, respectively, are known and only the UAV's 2–D position is estimated.

It is important to note that the channels between the UAVs and the cellular BTSs do not suffer from severe multipath, as a strong LOS component is usually observed in the received signal [60], [61]. In the case of severe multipath or non-LOS (NLOS) conditions, it is assumed that either (i) signal processing techniques at the SOP receiver level [24], [28], [56], [62]–[67] or (ii) measurement outlier rejection techniques [57] are used to mitigate mulitpath or exclude measurements with large errors due to multipath. Concepts of receiver autonomous integrity monitoring (RAIM) may also be used to exclude measurements with large errors, which can be considered as faulty measurements [68]–[71]. Alternatively, multipath error models may be used to predict and mitigate large measurement errors, either through multipath prediction maps [58], [72] or statistical models [73]. To this end, it is assumed in the rest of the paper that the effect of multipath has either (i) been mitigated or (ii) included in the measurement model (4).

III. Navigation with Carrier Phase Differential Cellular Measurements

This section develops the CD-cellular navigation framework and establishes guarantees on its achievable performance. The framework consists of two receivers in an environment comprising N cellular BTSs. The receivers are assumed to be listening to the same BTSs, with the BTS locations being known. The first receiver, referred to as the base (B), is assumed to have knowledge of its own position state (e.g., a stationary receiver deployed at a surveyed location or a high-flying aerial vehicle with access to GNSS). The second receiver, referred to as the rover UAV (U), does not know its position and aims to navigate using the CD-cellular framework. The base communicates its own position and carrier phase observables with the rover. Fig. 1 illustrates the base/rover framework.

A. CD-Cellular Measurement Model

In what follows, the objective is to estimate the rover's position, which will be achieved by double-differencing the measurements (4). It is subsequently assumed that the UAV and the base are within the same sector of a particular BTS. As such, there will be clock bias discrepancies due to sector mismatch

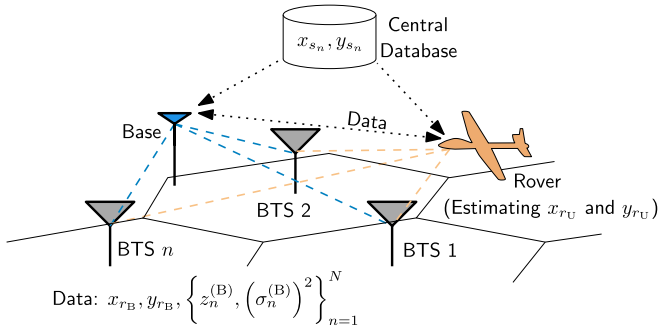

Fig. 1. CD-cellular base/rover framework.

[20]. Without loss of generality, let the measurements to the first SOP be taken as references to form the single difference

$$z_{n,1}^{(i)}(k) \triangleq z_n^{(i)}(k) - z_1^{(i)}(k), \tag{6}$$

for $n = 2, \ldots, N$. Subsequently, define the double difference between U and B as

$$\begin{aligned} z_{n,1}^{(\mathrm{U,B})}(k) &\triangleq z_{n,1}^{(\mathrm{U})}(k) - z_{n,1}^{(\mathrm{B})}(k) \\ &\quad + \sqrt{\|\boldsymbol{r}_{r_\mathrm{B}}(k) - \boldsymbol{r}_{s_n}\|_2^2 + \Delta z_{r_\mathrm{B},s_n}^2(k)} \\ &\quad - \sqrt{\|\boldsymbol{r}_{r_\mathrm{B}}(k) - \boldsymbol{r}_{s_1}\|_2^2 + \Delta z_{r_\mathrm{B},s_1}^2(k)} \\ &\triangleq h_{n,1}^{(\mathrm{U})}(k) + \lambda N_{n,1}^{(\mathrm{U,B})} + v_{n,1}^{(\mathrm{U,B})}(k), \end{aligned} \tag{7}$$

where $h_{n,1}{}^{(\mathrm{U})}(k) \triangleq \sqrt{\|\boldsymbol{r}_{r_\mathrm{U}}(k) - \boldsymbol{r}_{s_n}\|_2^2 + \Delta z_{r_\mathrm{U},s_n}^2(k)} - \sqrt{\|\boldsymbol{r}_{r_\mathrm{U}}(k) - \boldsymbol{r}_{s_1}\|_2^2 + \Delta z_{r_\mathrm{U},s_1}^2(k)}$, $N_{n,1}^{(\mathrm{U,B})} \triangleq N_n^{(\mathrm{U})} - N_n^{(\mathrm{B})} - N_1^{(\mathrm{U})} + N_1^{(\mathrm{B})}$, $v_{n,1}^{(\mathrm{U,B})}(k) \triangleq v_n^{(\mathrm{U})}(k) - v_n^{(\mathrm{B})}(k) - v_1^{(\mathrm{U})}(k) + v_1^{(\mathrm{B})}(k)$, and $n = 2, \ldots, N$. Note that (7) holds only when the UAV and base carrier phase measurements are synchronized. Synchronization is done using the cellular system time. The detected reference signals are used to synchronize the measurements from both receivers. Synchronization errors between the base and UAV receivers translate to differencing carrier phase measurements shifted in time. As such, the residual error in this case will be a function of the synchronization error Δt, the UAV speed v, and the receiver drifts $\dot{\delta} t$. It can be shown that the residual CD-cellular measurement error Δz due to synchronization errors between the base and rover is bounded according to

$$|\Delta z| \leq 2(v_{\max} + \dot{\delta} t_{\max})\Delta t, \tag{8}$$

where $v_{\max}$ is the maximum UAV speed and $\dot{\delta} t_{\max}$ is the maximum clock drift. It is shown in [44] that in typical open semi-urban cells, the synchronization error is less than 60 μs. As such, for $v_{\max} = 14$ m/s, which is considered high for small UAVs, and a 150 Hz drift at a carrier frequency of 882.75 MHz for the receiver clocks, which was observed from experimental data, the residual errors in the CD-cellular measurement will be less than 8 mm according to (8). Therefore, full synchronization is assumed. In vector form, the measurement model (7) becomes

$$\boldsymbol{z}_{\mathrm{U,B}}(k) \triangleq \boldsymbol{h}\left[\boldsymbol{r}_{r_\mathrm{U}}(k)\right] + \lambda \boldsymbol{N} + \boldsymbol{v}_{\mathrm{U,B}}(k), \tag{9}$$

where

$$\boldsymbol{z}_{\mathrm{U,B}}(k) \triangleq \left[z_{2,1}^{(\mathrm{U,B})}(k), \ldots, z_{N,1}^{(\mathrm{U,B})}(k)\right]^{\mathsf{T}}$$

$$\boldsymbol{h}\left[\boldsymbol{r}_{r_{\mathrm{U}}}(k)\right] \triangleq \left[h_{2,1}^{(\mathrm{U})}(k), \ldots, h_{N,1}^{(\mathrm{U})}(k)\right]^{\mathsf{T}}$$

$$\boldsymbol{N} \triangleq \left[N_{2,1}^{(\mathrm{U,B})}, \ldots, N_{N,1}^{(\mathrm{U,B})}\right]^{\mathsf{T}}$$

$$\boldsymbol{v}_{\mathrm{U,B}}(k) \triangleq \left[v_{2,1}^{(\mathrm{U,B})}(k), \ldots, v_{N,1}^{(\mathrm{U,B})}(k)\right]^{\mathsf{T}},$$

where $\boldsymbol{v}_{\mathrm{U,B}}(k)$ has a covariance $\mathbf{R}_{\mathrm{U,B}}(k)$, which can be readily shown to be

$$\mathbf{R}_{\mathrm{U,B}}(k) = \mathbf{R}^{(1)}(k) + \left[\sigma_1^{(\mathrm{U,B})}(k)\right]^2 \mathbf{1}_{N-1}\mathbf{1}_{N-1}^{\mathsf{T}}, \tag{10}$$

where $[\sigma_1^{(\mathrm{U,B})}(k)]^2 \triangleq [[\sigma_1^{(\mathrm{B})}(k)]^2 + [\sigma_1^{(\mathrm{U})}(k)]^2]$,

$$\mathbf{R}^{(1)}(k) \triangleq \mathrm{diag}\left[\left[\sigma_2^{(\mathrm{B})}(k)\right]^2 + \left[\sigma_2^{(\mathrm{U})}(k)\right]^2, \ldots, \left[\sigma_N^{(\mathrm{B})}(k)\right]^2 + \left[\sigma_N^{(\mathrm{U})}(k)\right]^2\right],$$

and $\mathbf{1}_{N-1}$ is an $(N-1)\times 1$ vector of ones. Note that the vector $\boldsymbol{N}$ is now a vector of $N-1$ integers and has to be solved for along with the rover UAV's position $\boldsymbol{r}_{r_{\mathrm{U}}}$. The next subsections present a framework to obtain a navigation solution with CD-cellular measurements.

B. Navigation Strategy

It is important to first establish the navigation strategy employed by the UAV. To this end, assume CD-cellular measurements are given at $k = 0, 1, 2, \ldots$. It is desired that, with probability greater than $1-\alpha$, the 2-norm of the position error be less than a desired threshold ζ for all $k \geq k_\zeta$. Let $\delta\boldsymbol{r}_{r_{\mathrm{U}}}(k)$ denote the position error at time-step k. Then, it is desired that

$$\Pr\left[\|\delta\boldsymbol{r}_{r_{\mathrm{U}}}(k)\|_2^2 \leq \zeta^2\right] \geq 1-\alpha, \quad \forall\, k \geq k_\zeta. \tag{11}$$

For $k < k_\zeta$, the UAV will use an EKF to produce a "rough" estimate of its position and the integer ambiguities. Measurements at $k=0$ and $k=1$ are used to initialize the EKF. Then, at $k = k_\zeta$, a batch weighted nonlinear least-squares (B-WNLS) estimator for all measurements from $k=0$ to k_ζ is used to obtain an estimate of the integer ambiguities that guarantees (11) for $k \geq k_\zeta$. The EKF solution is used to initialize the B-WNLS. For $k > k_\zeta$, the UAV will solve for its position using $\boldsymbol{z}_{\mathrm{U,B}}(k)$ and the estimated ambiguities through a point solution weighted nonlinear least-squares (PS-WNLS). The time-step k_ζ is determined on-the-fly by the UAV via the test developed in the remaining of this section. Fig. 2 summarizes the aforementioned navigation strategy.

The blocks in Fig. 2 are subsequently described.

C. EKF Model and Initialization

Define the vector $\boldsymbol{x}_{\mathrm{EKF}} \triangleq [\boldsymbol{r}_{r_{\mathrm{U}}}^{\mathsf{T}}, \dot{\boldsymbol{r}}_{r_{\mathrm{U}}}^{\mathsf{T}}, \boldsymbol{N}^{\mathsf{T}}]^{\mathsf{T}}$ as the state vector to be estimated by the EKF, where $\dot{\boldsymbol{r}}_{r_{\mathrm{U}}}^{\mathsf{T}}$ is the 2–D velocity vector of the UAV. The UAV's position and velocity states are assumed

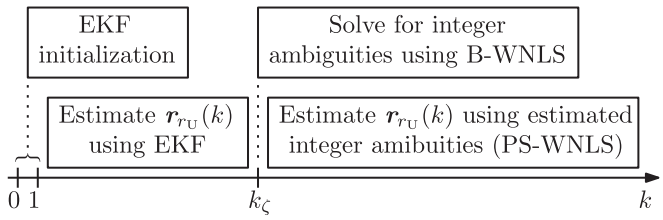

Fig. 2. Diagram of the proposed CD-cellular navigation strategy.

to evolve according to a velocity random walk model [31]. Note that only the float solution of $\boldsymbol{N}$ is estimated in the EKF, i.e., the integer constraint is relaxed. The EKF will produce an estimate $\hat{\boldsymbol{x}}_{\mathrm{EKF}}(k|j)$, i.e., an estimate of $\boldsymbol{x}_{\mathrm{EKF}}(k)$ using all measurements $\boldsymbol{z}_{\mathrm{U,B}}(k)$ up to time-step $j \leq k$, along with an estimation error covariance $\mathbf{P}_{\mathrm{EKF}}(k|j) \triangleq \mathbb{E}[\tilde{\boldsymbol{x}}_{\mathrm{EKF}}(k|j)\tilde{\boldsymbol{x}}_{\mathrm{EKF}}^{\mathsf{T}}(k|j)]$ where $\tilde{\boldsymbol{x}}_{\mathrm{EKF}}(k|j) \triangleq \boldsymbol{x}_{\mathrm{EKF}}(k) - \hat{\boldsymbol{x}}_{\mathrm{EKF}}(k|j)$ is the estimation error. The UAV's random walk dynamics and the measurement model in (9) are used to derive the EKF time-update and measurement-update equations. The EKF initialization is discussed next. Note that the measurement $\boldsymbol{z}_{\mathrm{U,B_{ini}}} \triangleq [\boldsymbol{z}_{\mathrm{U,B}}^{\mathsf{T}}(0), \boldsymbol{z}_{\mathrm{U,B}}^{\mathsf{T}}(1)]^{\mathsf{T}}$ may be parameterized as

$$\boldsymbol{z}_{\mathrm{U,B_{ini}}} = \begin{bmatrix}\boldsymbol{z}_{\mathrm{U,B}}(0)\\ \boldsymbol{z}_{\mathrm{U,B}}(1)\end{bmatrix} = \boldsymbol{h}_{\mathrm{ini}}\left[\boldsymbol{x}_{\mathrm{EKF}}(1)\right] + \boldsymbol{v}_{\mathrm{U,B_{ini}}}, \tag{12}$$

$$\boldsymbol{h}_{\mathrm{ini}}\left[\boldsymbol{x}_{\mathrm{EKF}}(1)\right] \triangleq \begin{bmatrix}\boldsymbol{h}\left[\boldsymbol{r}_{r_{\mathrm{U}}}(1) - T\dot{\boldsymbol{r}}_{r_{\mathrm{U}}}(1)\right] + \lambda\boldsymbol{N}\\ \boldsymbol{h}\left[\boldsymbol{r}_{r_{\mathrm{U}}}(1)\right] + \lambda\boldsymbol{N}\end{bmatrix},$$

where T is the sampling time and $\boldsymbol{v}_{\mathrm{U,B_{ini}}} \triangleq [\boldsymbol{v}_{\mathrm{U,B}}^{\mathsf{T}}(0), \boldsymbol{v}_{\mathrm{U,B}}^{\mathsf{T}}(1)]^{\mathsf{T}}$ is the overall initial measurement noise, which is modeled as a zero-mean Gaussian random vector with covariance $\mathbf{R}_{\mathrm{ini}} \triangleq \mathrm{diag}[\mathbf{R}_{\mathrm{U,B}}(0), \mathbf{R}_{\mathrm{U,B}}(1)]$. The measurement equation in (12) can be solved in a weighted nonlinear least-squares (WNLS) estimator (e.g., using the Gauss-Newton algorithm) with a weighting matrix $\mathbf{R}_{\mathrm{ini}}^{-1}$ [74]. Solving the WNLS yields an estimate of $\boldsymbol{x}_{\mathrm{EKF}}(1)$, denoted $\hat{\boldsymbol{x}}_{\mathrm{EKF,ini}}$, and an associated estimation error covariance, denoted $\mathbf{P}_{\mathrm{EKF,ini}}$. Finally, the EKF initial estimate and estimation error covariance are initialized according to

$$\hat{\boldsymbol{x}}_{\mathrm{EKF}}(1|1) \equiv \hat{\boldsymbol{x}}_{\mathrm{EKF,ini}}, \quad \mathbf{P}_{\mathrm{EKF}}(1|1) \equiv \mathbf{P}_{\mathrm{EKF,ini}}. \tag{13}$$

Note that the size of $\boldsymbol{z}_{\mathrm{U,B_{ini}}}$ must be greater than or equal to the size of $\boldsymbol{x}_{\mathrm{EKF}}$ to perform the steps described above, i.e., N must satisfy $K_B(N-1) \geq ((N-1)+4)$, where K_B is the batch size. In the case where $K_B = 2$, as in (12), then N must be 5 or more. If $N < 5$, then the batch size must be increased. However, N must satisfy $N \geq 2$, otherwise the CD-cellular measurements cannot be formed.

D. B-WNLS Solution

When $k = k_\zeta$, the B-WNLS estimate of the UAV's position and the integer ambiguities is computed. Define the collection of carrier phase measurements from time-step 0 to k_ζ as

$$\mathbf{z}_{\mathrm{U,B}}^{k_\zeta} \triangleq \left[\boldsymbol{z}_{\mathrm{U,B}}^{\mathsf{T}}(0), \ldots, \boldsymbol{z}_{\mathrm{U,B}}^{\mathsf{T}}(k_\zeta)\right]^{\mathsf{T}}, \tag{14}$$

which can be expressed as

$$\mathbf{z}_{\mathrm{U,B}}^{k_\zeta} = \mathbf{h}\left[\mathbf{r}_{r_\mathrm{U}}^{k_\zeta}\right] + \lambda \bar{\mathbf{I}}^{k_\zeta} \boldsymbol{N} + \mathbf{v}_{\mathrm{U,B}}^{k_\zeta}, \tag{15}$$

$$\mathbf{r}_{r_\mathrm{U}}^{k_\zeta} \triangleq \begin{bmatrix} \boldsymbol{r}_{r_\mathrm{U}}(0) \\ \vdots \\ \boldsymbol{r}_{r_\mathrm{U}}(k_\zeta) \end{bmatrix}, \ \mathbf{v}_{\mathrm{U,B}}^{k_\zeta} \triangleq \begin{bmatrix} \boldsymbol{v}_{\mathrm{U,B}}(0) \\ \vdots \\ \boldsymbol{v}_{\mathrm{U,B}}(k_\zeta) \end{bmatrix},$$

$$\mathbf{h}\left[\mathbf{r}_{r_\mathrm{U}}^{k_\zeta}\right] \triangleq \begin{bmatrix} \boldsymbol{h}\left[\boldsymbol{r}_{r_\mathrm{U}}(0)\right] \\ \vdots \\ \boldsymbol{h}\left[\boldsymbol{r}_{r_\mathrm{U}}(k_\zeta)\right] \end{bmatrix}, \ \bar{\mathbf{I}}^{k_\zeta} \triangleq \begin{bmatrix} \mathbf{I}_{(N-1)\times(N-1)} \\ \vdots \\ \mathbf{I}_{(N-1)\times(N-1)} \end{bmatrix},$$

where $\mathbf{v}_{\mathrm{U,B}}^{k_\zeta}$ is the overall carrier phase measurement noise with covariance $\mathbf{R}_{\mathrm{U,B}}^{k_\zeta} \triangleq \mathrm{diag}[\mathbf{R}_{\mathrm{U,B}}(0), \ldots, \mathbf{R}_{\mathrm{U,B}}(k_\zeta)]$.

Let $\boldsymbol{x}_{\mathrm{B-WNLS}}^{k_\zeta} \triangleq [(\mathbf{r}_{r_\mathrm{U}}^{k_\zeta})^\mathsf{T}, \boldsymbol{N}^\mathsf{T}]^\mathsf{T}$ denote the parameters to be estimated. A B-WNLS estimator with weight matrix $(\mathbf{R}_{\mathrm{U,B}}^{k_\zeta})^{-1}$ is used to obtain an estimate $\hat{\boldsymbol{x}}_{\mathrm{B-WNLS}}^{k_\zeta} \triangleq [(\hat{\mathbf{r}}_{r_\mathrm{U}}^{k_\zeta})^\mathsf{T}, (\hat{\boldsymbol{N}}^{k_\zeta})^\mathsf{T}]^\mathsf{T}$ of $\boldsymbol{x}_{\mathrm{B-WNLS}}^{k}$ and an associated estimation error covariance $\mathbf{P}_{\mathrm{B-WNLS}}^{k_\zeta}$, given by

$$\mathbf{P}_{\mathrm{B-WNLS}}^{k_\zeta} = \begin{bmatrix} \mathbf{P}_{\mathbf{r}_\mathrm{U}}^{k_\zeta} & \mathbf{P}_{\mathbf{r}_\mathrm{U},\boldsymbol{N}}^{k_\zeta} \\ \left(\mathbf{P}_{\mathbf{r}_\mathrm{U},\boldsymbol{N}}^{k_\zeta}\right)^\mathsf{T} & \mathbf{P}_{\boldsymbol{N}}^{k_\zeta} \end{bmatrix}. \tag{16}$$

Note the dependency of $\hat{\boldsymbol{N}}^{k_\zeta}$ on k_ζ.

The vector $\boldsymbol{N}$ consists of integers; however, its estimate, the vector $\hat{\boldsymbol{N}}^{k_\zeta}$, is not necessarily a vector of integers. As such, the vector $\hat{\boldsymbol{N}}^{k_\zeta}$ must be "fixed" to the correct integers. This is achieved using the LAMBDA method [49], which produces the vector of fixed integers denoted by $\check{\boldsymbol{N}}^{k_\zeta}$ obtained from the float solution $\hat{\boldsymbol{N}}^{k_\zeta}$ and $\mathbf{P}_{\boldsymbol{N}}^{k_\zeta}$. Specifically, the vector $\check{\boldsymbol{N}}^{k_\zeta}$ is defined as

$$\check{\boldsymbol{N}}^{k_\zeta} \triangleq \underset{\boldsymbol{N}\in\mathbb{Z}^{N-1}}{\mathrm{argmin}} \left[\left(\hat{\boldsymbol{N}}^{k_\zeta} - \boldsymbol{N}\right)^\mathsf{T} \left(\mathbf{P}_{\boldsymbol{N}}^{k_\zeta}\right)^{-1} \left(\hat{\boldsymbol{N}}^{k_\zeta} - \boldsymbol{N}\right)\right], \tag{17}$$

where $\mathbb{Z}$ is the set of integers. After fixing the integer ambiguities, the UAV's fixed position estimates $\check{\mathbf{r}}_{r_\mathrm{U}}^{k}$ are obtained according to

$$\check{\mathbf{r}}_{r_\mathrm{U}}^{k_\zeta} = \hat{\mathbf{r}}_{r_\mathrm{U}}^{k_\zeta} - \mathbf{P}_{\mathbf{r}_\mathrm{U},\boldsymbol{N}}^{k_\zeta} \mathbf{P}^{k_\zeta\,-1}_{\boldsymbol{N}} \left(\hat{\boldsymbol{N}}^{k_\zeta} - \check{\boldsymbol{N}}^{k_\zeta}\right). \tag{18}$$

Note that the B-WNLS solution is initialized with the EKF estimates of the UAV positions and ambiguities.

E. PS-WNLS

Once the integer ambiguities are determined, the carrier phase measurements at time-step $k \geq k_\zeta$ are used to determine the point solution $\hat{\boldsymbol{r}}_{r_\mathrm{U}}(k)$ and an associated estimation error covariance $\mathbf{P}_{\boldsymbol{r}_\mathrm{U}}(k)$ using a WNLS, i.e., the estimate of $\boldsymbol{r}_{r_\mathrm{U}}(k)$ using $\boldsymbol{z}_{\mathrm{U,B}}(k)$ and $\tilde{\boldsymbol{N}}^{k_\zeta}$ through a WNLS. To this end, define the integer ambiguity estimation error as $\tilde{\boldsymbol{N}}^{k_\zeta} \triangleq \boldsymbol{N} - \check{\boldsymbol{N}}^{k_\zeta}$. Hence, the carrier phase measurement vector for $k \geq k_\zeta$ can be parameterized by

$$\boldsymbol{z}_{\mathrm{U,B}}(k) \triangleq \boldsymbol{h}\left[\boldsymbol{r}_{r_\mathrm{U}}(k)\right] + \lambda \check{\boldsymbol{N}}^{k_\zeta} + \lambda \tilde{\boldsymbol{N}}^{k_\zeta} + \boldsymbol{v}_{\mathrm{U,B}}(k). \tag{19}$$

The difference between (9) and (19) is that now an estimate of $\boldsymbol{N}$ is known to the UAV, and it can therefore estimate its position vector instantaneously using $\boldsymbol{z}_{\mathrm{U,B}}(k)$. However, $\lambda\tilde{\boldsymbol{N}}^{k_\zeta}$ is now introduced as an additional measurement error, where $\tilde{\boldsymbol{N}}^{k_\zeta}$ can be modeled as a zero-mean random vector with covariance $\mathbf{P}_{\boldsymbol{N}}^{k_\zeta}$. The weight matrix in the PS-WNLS is chosen to be

$$\boldsymbol{\Sigma}^{-1}(k) \triangleq \left[\lambda^2 \mathbf{P}_{\boldsymbol{N}}^{k_\zeta} + \mathbf{R}_{\mathrm{U,B}}(k)\right]^{-1}. \tag{20}$$

In the following sections, k_ζ is determined to satisfy (11) $\forall\, k \geq k_\zeta$. To this end, the position error is first probabilistically upper bounded and a test on k is derived to determine when (11) will hold.

F. Probabilistic Position Error Upper Bound

The carrier phase measurement noise standard deviation calculated from (5) is on the order of a 1.5 cm for a carrier-to-noise ratio of 35 dB-Hz and a wavelength of 34 cm (800 MHz cellular band). Moreover, typical carrier-to-noise ratios for cellular signals are observed to be much higher than 35 dB-Hz for low-altitude receivers, reaching 60 dB-Hz or more in the case of LTE and 5G signal [37]. As such, it is assumed that the contribution of $\boldsymbol{v}_{\mathrm{U,B}}(k)$ to the estimation error is insignificant compared to $\tilde{\boldsymbol{N}}^{k_\zeta}$. The position error due to $\tilde{\boldsymbol{N}}^{k_\zeta}$ can be approximated by

$$\delta\boldsymbol{r}_{r_\mathrm{U}}(k) = \lambda \left[\tilde{\mathbf{G}}^\mathsf{T}(k)\boldsymbol{\Sigma}^{-1}(k)\tilde{\mathbf{G}}(k)\right]^{-1} \tilde{\mathbf{G}}^\mathsf{T}(k)\boldsymbol{\Sigma}^{-1}(k)\tilde{\boldsymbol{N}}^{k_\zeta}, \tag{21}$$

$$\tilde{\mathbf{G}}(k) = \begin{bmatrix} \frac{\hat{\boldsymbol{r}}_{r_\mathrm{U}}^\mathsf{T}(k) - \boldsymbol{r}_{s_2}^\mathsf{T}}{\sqrt{\left\|\hat{\boldsymbol{r}}_{r_\mathrm{U}}(k) - \boldsymbol{r}_{s_2}\right\|_2^2 + \Delta z_{r_\mathrm{U},s_2}^2(k)}} - \frac{\hat{\boldsymbol{r}}_{r_\mathrm{U}}^\mathsf{T}(k) - \boldsymbol{r}_{s_1}^\mathsf{T}}{\sqrt{\left\|\hat{\boldsymbol{r}}_{r_\mathrm{U}}(k) - \boldsymbol{r}_{s_1}\right\|_2^2 + \Delta z_{r_\mathrm{U},s_1}^2(k)}} \\ \vdots \\ \frac{\hat{\boldsymbol{r}}_{r_\mathrm{U}}^\mathsf{T}(k) - \boldsymbol{r}_{s_N}^\mathsf{T}}{\sqrt{\left\|\hat{\boldsymbol{r}}_{r_\mathrm{U}}(k) - \boldsymbol{r}_{s_N}\right\|_2^2 + \Delta z_{r_\mathrm{U},s_N}^2(k)}} - \frac{\hat{\boldsymbol{r}}_{r_\mathrm{U}}^\mathsf{T}(k) - \boldsymbol{r}_{s_1}^\mathsf{T}}{\sqrt{\left\|\hat{\boldsymbol{r}}_{r_\mathrm{U}}(k) - \boldsymbol{r}_{s_1}\right\|_2^2 + \Delta z_{r_\mathrm{U},s_1}^2(k)}} \end{bmatrix}. \tag{22}$$

The estimation error covariance associated with the position estimate is expressed as

$$\mathbf{P}_{\boldsymbol{r}_\mathrm{U}}(k) = \left[\tilde{\mathbf{G}}^\mathsf{T}(k)\boldsymbol{\Sigma}^{-1}(k)\tilde{\mathbf{G}}(k)\right]^{-1}. \tag{23}$$

In what follows, the time argument will be omitted for compactness of notation. Let $\boldsymbol{\Sigma}^{\frac{1}{2}}$ denote a square root of $\boldsymbol{\Sigma}$. Using the submultiplicative property of the 2-norm, it can be shown from (21) that

$$\|\delta\boldsymbol{r}_{r_\mathrm{U}}\|_2^2 \leq \lambda^2 \left\|\left[\tilde{\mathbf{G}}^\mathsf{T}\boldsymbol{\Sigma}^{-1}\tilde{\mathbf{G}}\right]^{-1} \tilde{\mathbf{G}}^\mathsf{T}\boldsymbol{\Sigma}^{-\frac{1}{2}}\right\|_2^2 \left\|\boldsymbol{\Sigma}^{-\frac{1}{2}}\tilde{\boldsymbol{N}}^{k_\zeta}\right\|_2^2. \tag{24}$$

Using the fact that the square of the 2-norm of some real matrix $\mathbf{A}$ is the maximum eigenvalue of $\mathbf{A}\mathbf{A}^\mathsf{T}$ [75, p. 266 & 341], denoted by $\lambda_{\max}(\mathbf{A}\mathbf{A}^\mathsf{T})$, the term $\|[\tilde{\mathbf{G}}^\mathsf{T}\boldsymbol{\Sigma}^{-1}\tilde{\mathbf{G}}]^{-1}\tilde{\mathbf{G}}^\mathsf{T}\boldsymbol{\Sigma}^{-\frac{1}{2}}\|_2^2$ is calculated to be

$$\begin{aligned} \left\|\left[\tilde{\mathbf{G}}^\mathsf{T}\boldsymbol{\Sigma}^{-1}\tilde{\mathbf{G}}\right]^{-1} \tilde{\mathbf{G}}^\mathsf{T}\boldsymbol{\Sigma}^{-\frac{1}{2}}\right\|_2^2 &= \lambda_{\max}\left(\left[\tilde{\mathbf{G}}^\mathsf{T}\boldsymbol{\Sigma}^{-1}\tilde{\mathbf{G}}\right]^{-1}\right) \\ &= \lambda_{\max}\left(\mathbf{P}_{\boldsymbol{r}_\mathrm{U}}\right), \end{aligned} \tag{25}$$

where the last equality follows from (23). Subsequently, $\|\delta \boldsymbol{r}_{r_{\mathrm{U}}}\|_2^2$ can be further bounded according to

$$\|\delta \boldsymbol{r}_{r_{\mathrm{U}}}\|_2^2 \leq \lambda^2 \lambda_{\max}\left(\mathbf{P}_{\boldsymbol{r}_{\mathrm{U}}}\right) \left\|\boldsymbol{\Sigma}^{-\frac{1}{2}} \tilde{\boldsymbol{N}}^{k_\zeta}\right\|_2^2. \tag{26}$$

Note that

$$\begin{aligned}\mathbf{P}_{\boldsymbol{r}_{\mathrm{U}}} &\preceq \lambda_{\max}\left(\boldsymbol{\Sigma}\right)\left(\tilde{\mathbf{G}}^{\mathsf{T}}\tilde{\mathbf{G}}\right)^{-1} \\ &\preceq \lambda_{\max}\left(\boldsymbol{\Sigma}\right) \underbrace{\operatorname{trace}\left[\left(\tilde{\mathbf{G}}^{\mathsf{T}}\tilde{\mathbf{G}}\right)^{-1}\right]}_{\triangleq \mathrm{HDOP}^2} \mathbf{I}_{2\times 2},\end{aligned} \tag{27}$$

where the horizontal dilution of precision (HDOP) depends on the current geometry between the UAV and the cellular BTSs. With probability β, the HDOP is probabilistically upper bounded according to

$$\Pr\left[\mathrm{HDOP} \leq \mathrm{HDOP}_{\max}\right] = \beta, \tag{28}$$

where $\mathrm{HDOP}_{\max}$ can be calculated in advance from the known cellular BTS using stochastic geometry models, as discussed in the next subsection. Subsequently, $\lambda_{\max}(\mathbf{P}_{\boldsymbol{r}_{\mathrm{U}}})$ can be bounded according to

$$\lambda_{\max}\left(\mathbf{P}_{\boldsymbol{r}_{\mathrm{U}}}\right) \leq \lambda_{\max}\left(\boldsymbol{\Sigma}\right) \mathrm{HDOP}_{\max}^2, \tag{29}$$

which in turn implies that with a probability greater than β, the following holds

$$\|\delta \boldsymbol{r}_{r_{\mathrm{U}}}\|_2^2 \leq \lambda^2 \lambda_{\max}\left(\boldsymbol{\Sigma}\right) \mathrm{HDOP}_{\max}^2 \left\|\boldsymbol{\Sigma}^{-\frac{1}{2}} \tilde{\boldsymbol{N}}^{k_\zeta}\right\|_2^2. \tag{30}$$

G. Determination of $HDOP_{max}$

In order to determine the distribution of HDOP and hence $\mathrm{HDOP}_{\max}$, stochastic geometry is used to model the relative geometry between the UAV and BTSs. Specifically, the BTS positions are modeled as a binomial point process (BPP) and the total number of hearable BTSs is assumed to be known [76], [77]. The BTS position distribution is parameterized by the minimum and maximum hearable distance to a BTS, denoted by $d_{\min}$ and $d_{\max}$, respectively. However, the HDOP can be parameterized by the bearing angles only; hence, the dependency on $d_{\min}$ and $d_{\max}$ is eliminated. Then, several realizations of the BTS bearing angles are realized for a given value of N and the empirical cumulative density function (cdf) of the HDOP is characterized. Finally, the value $\mathrm{HDOP}_{\max}$ is identified from the emprical cdf for a desired β. Fig. 3(a) illustrates a realization of the BPP for $N = 15$ ($d_{\min} = 50$ m and $d_{\max} = 5000$ m) and Fig. 3(b) shows $\mathrm{HDOP}_{\max}$ for various N and β obtained from 10^5 BPP realizations.

H. Probabilistic Integer Ambiguity Error Upper Bound

With a probability greater than $1-p$, $\tilde{\boldsymbol{N}}^{k_\zeta}$ will be within the confidence region defined as

$$\left(\tilde{\boldsymbol{N}}^{k_\zeta}\right)^{\mathsf{T}} \left(\mathbf{P}_{\boldsymbol{N}}^{k_\zeta}\right)^{-1} \tilde{\boldsymbol{N}}^{k_\zeta} \leq \gamma(p), \tag{31}$$

where $\gamma(p) \triangleq f^{-1}_{\chi^2,N-1}(1-p)$ and $f^{-1}_{\chi^2,M}(\cdot)$ is the inverse cdf of a chi-square distributed random variable with M degrees of freedom. Note that the left-hand side of (31) would not be chi-square distributed in the presence of unmodeled errors such as multipath biases due to deep fading or cycle slips. In such cases, the measurement noise variance must be inflated to overbound these unmodeled errors. This can be investigated further in future work. By defining

$$\bar{\mathbf{P}}_{\boldsymbol{N}}^{k_\zeta} \triangleq \boldsymbol{\Sigma}^{-\frac{1}{2}} \mathbf{P}_{\boldsymbol{N}}^{k_\zeta} \boldsymbol{\Sigma}^{-\frac{1}{2}}, \tag{32}$$

the inequality in (31) may be re-written as

$$\left(\boldsymbol{\Sigma}^{-\frac{1}{2}} \tilde{\boldsymbol{N}}^{k_\zeta}\right)^{\mathsf{T}} \left(\bar{\mathbf{P}}_{\boldsymbol{N}}^{k_\zeta}\right)^{-1} \boldsymbol{\Sigma}^{-\frac{1}{2}} \tilde{\boldsymbol{N}}^{k_\zeta} \leq \gamma(p). \tag{33}$$

Note that (33) implies the inequality

$$\Pr\left[\left\|\boldsymbol{\Sigma}^{-\frac{1}{2}} \tilde{\boldsymbol{N}}^{k_\zeta}\right\|_2^2 \leq \lambda_{\max}\left(\bar{\mathbf{P}}_{\boldsymbol{N}}^{k_\zeta}\right) \gamma(p)\right] \geq 1-p. \tag{34}$$

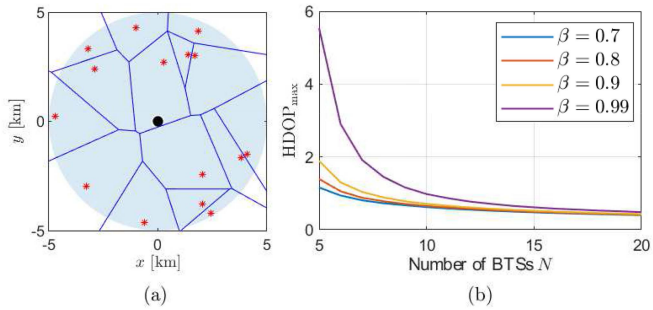

Fig. 3. (a) Voronoi diagram for a realization of the BPP for $N = 15$. The red asterisks indicate the BTS locations and the black disc at the origin inidcates the UAV location. The shaded blue area is the ring defined between $d_{\min}$ and $d_{\max}$. (b) $\mathrm{HDOP}_{\max}$ that satisfies $\Pr[\mathrm{HDOP} \leq \mathrm{HDOP}_{\max}] = \beta$ for various N and β values. The empirical cdf of the HDOP was calculated from 10^5 BPP realizations.

I. Eigenvalue Test for Batch Size Determination

Assuming that the HDOP and $\tilde{\boldsymbol{N}}$ are independent, the following inequality holds

$$\begin{aligned}&\Pr\left[\|\delta \boldsymbol{r}_{r_{\mathrm{U}}}\|_2^2 \leq \lambda^2 \lambda_{\max}(\boldsymbol{\Sigma})\, \mathrm{HDOP}_{\max}^2 \lambda_{\max}\left(\bar{\mathbf{P}}_{\boldsymbol{N}}^{k_\zeta}\right) \gamma(p)\right] \\ &\quad \geq \beta(1-p).\end{aligned} \tag{35}$$

Recall that (11) is desired; therefore, satisfying

$$\begin{aligned}&\lambda^2 \lambda_{\max}\left(\boldsymbol{\Sigma}\right) \mathrm{HDOP}_{\max}^2 \lambda_{\max}\left(\bar{\mathbf{P}}_{\boldsymbol{N}}^{k_\zeta}\right) \gamma(p) \leq \zeta^2 \\ &\qquad \Rightarrow \quad \lambda_{\min}\left(\left(\bar{\mathbf{P}}_{\boldsymbol{N}}^{k_\zeta}\right)^{-1}\right) \geq g\left(\zeta, p\right),\end{aligned} \tag{36}$$

achieves (11), where $\lambda_{\min}(\mathbf{A})$ denotes the smallest eigenvalue of matrix $\mathbf{A}$, $g(\zeta,p) \triangleq (\frac{1}{\zeta^2})[\lambda^2 \lambda_{\max}(\boldsymbol{\Sigma}) \mathrm{HDOP}_{\max}^2 \gamma(p)]$, and $p = 1-(1-\alpha)/\beta$. Note that the inequality in (36) is in the form of a test that can be performed after each measurement is added to the batch filter.

Remark: It is easier to compute $(\bar{\mathbf{P}}_{\boldsymbol{N}}^{k_\zeta})^{-1}$ rather than $\bar{\mathbf{P}}_{\boldsymbol{N}}^{k_\zeta}$ without having to solve the batch WNLS; hence, the test is on $\lambda_{\min}((\bar{\mathbf{P}}_{\boldsymbol{N}}^{k_\zeta})^{-1})$. Appendix A shows that the inversion of 2×2 matrices only is needed to compute $(\bar{\mathbf{P}}_{\boldsymbol{N}}^{k_\zeta})^{-1}$.

IV. Experimental Results

This section presents experimental results demonstrating submeter-level UAV navigation results via the framework developed in this paper. As mentioned in Section III, only the 2–D position of the UAV is estimated as its altitude may be obtained using other sensors (e.g., altimeter). The UAV's position is estimated in the horizontal plane of an East-North-Up (ENU) frame centered at the average of the BTS positions. In the following experiments, the altitude of the UAV was obtained from its on-board navigation system. Alternatively, the UAV's altitude may be obtained from a barometric altimeter. Moreover, the noise equivalent bandwidths of the receivers' PLLs were set to $B_{\mathrm{U,PLL}} = B_{\mathrm{B,PLL}} = B_{\mathrm{PLL}} = 3$ Hz in all experiments and the measurement noise covariances were calculated according to (5).

A. Experimental Layout and Setup

In order to demonstrate the CD-cellular framework discussed in Section III, two Autel Robotics X-Star Premium UAVs were equipped each with an Ettus E312 universal software radio peripheral (USRP), a consumer-grade 800/1900 MHz cellular antenna, and a small consumer-grade GPS antenna to discipline the on-board oscillator for ground-truth collection. Note that one UAV acted as a base and the other as a navigating UAV. The base was mounted on a UAV since access to building roofs was restricted in the experiment area. The receivers were tuned to a 882.75 MHz carrier frequency (i.e., $\lambda = 33.96$ cm), which is a cellular CDMA channel allocated for the U.S. cellular provider Verizon Wireless. Samples of the received signals were stored for off-line post-processing. The cellular carrier phase measurements were given at a rate of 12.5 Hz, i.e., $T = 0.08$ s. The ground-truth reference for each UAV trajectory was taken from its on-board integrated navigation system, which uses GPS, an inertial measurement unit (IMU), and other sensors. The hovering horizontal precision of the Autel Robotics X-Star Premium UAVs are reported to be 2 m.

The navigating UAV's total traversed trajectory was 2.24 km, which was completed in 4 minutes with a total trajectory radius of 270 m. The trajectory radius is defined as the distance between the centre of the trajectory and the furthest point on the trajectory. Over the course of the experiment which took place in an open semi-urban environment and mulitpath-free, LOS conditions near Riverside, California, USA, the receivers were listening to 9 BTSs, whose 3–D positions were mapped prior to the experiment according to the framework in [78]. Some errors may arise due to uncertainties in the BTS positions, which were verified from Google Earth imagery. While the accuracy of Google Earth is not officially known, studies show that it is below 20 cm in the areas of interest [79]. A panorama of the environment from the UAV's vantage point is shown in Fig. 4, and the channel impulse response measured using the autocorrelation function of the CDMA shortcode for all 9 BTSs over 300 seconds is shown in Fig. 5. The curves in Fig. 5 demonstrate a dominant LOS component and nearly multipath-free conditions. Throughout the experiments, the UAV remained in the same BTS sectors as the base receiver. The CD-cellular measurements were used to estimate the navigating UAV's trajectory via the base/UAV framework developed in Section III. The experimental setup, the cellular BTS layout, and the true trajectory (from the UAV's on-board integrated navigation system) and estimated trajectory (from the proposed CD-cellular framework) of the navigating UAV are shown in Fig. 7. A plot of the carrier-to-noise ratios of all the BTSs measured by the rover and the time history of the delta ranges (deviation from the initial range) are given in Fig. 6(a) and Fig. 6(b), respectively. The base measured similar carrier-to-noise values.

Fig. 4. Panorama of the environment from the UAV's vantage point for the environment near Riverside, California, USA.

TABLE I
Experimental Results ($k_\zeta T = 120$ s)

	$k < k_\zeta$	$k \geq k_\zeta$	$\forall k$
Duration	120 s	120 s	240 s
Distance traveled	0.96 km	1.28 km	2.24 km
Trajectory radius	330 m	168 m	270 m
EKF RMSE	24.15 m	3.95 m	14.53 m
B–WNLS RMSE	65.79 cm	–	–
PS–WNLS RMSE	65.79 cm	74.83 cm	70.48 cm
No Test RMSE	–	–	12.26 m

B. Navigation Results

The probabilities β and α were set to 0.99 and 0.4, respectively, and the desired position error threshold was set to (i) $\zeta \equiv \zeta_1 = \sqrt{2}$ m and (ii) $\zeta \equiv \zeta_2 = 3$ m. For these parameters, $k_{\zeta_1} T$ was found to be 120 s and $k_{\zeta_2} T$ was found to be 99 s. The position RMSE for $k < k_{\zeta_1}$ was found to be 24.15 m (from the EKF), and 74.89 cm for $k \geq k_{\zeta_1}$ (from the PS-WNLS, after resolving the integer ambiguities through the B-WNLS). The estimated trajectories are also shown in Fig. 7 and the position error and associated $\pm 3\sigma$ bounds are shown in Fig. 8. Similarly, the position RMSE for $k < k_{\zeta_2}$ was found to be 24.15 m (from the EKF), and 2.65 m for $k \geq k_{\zeta_2}$. The time history of $\lambda_{\min}((\bar{\mathbf{P}}_{\boldsymbol{N}}^{k_\zeta})^{-1})$ is shown in Fig. 9(a) along with $g(\zeta_1, p)$ and $g(\zeta_2, p)$, and the empirical cdfs of the position RMSE for $k \geq 0$ and for $k \geq k_\zeta$ (after resolving the ambiguities through the B-WNLS) are shown in Fig. 9(b) and (c) for ζ_1 and ζ_2, respectively. The position RMSEs for each part of the trajectory are shown in Tables I and II for ζ_1 and ζ_2, respectively. It can be seen from Fig. 9(b) that $\Pr[\|\delta \boldsymbol{r}_{r_{\mathrm{U}}}\|_2^2 \leq \zeta_1^2] = 0.62 \geq 1 - \alpha$ and

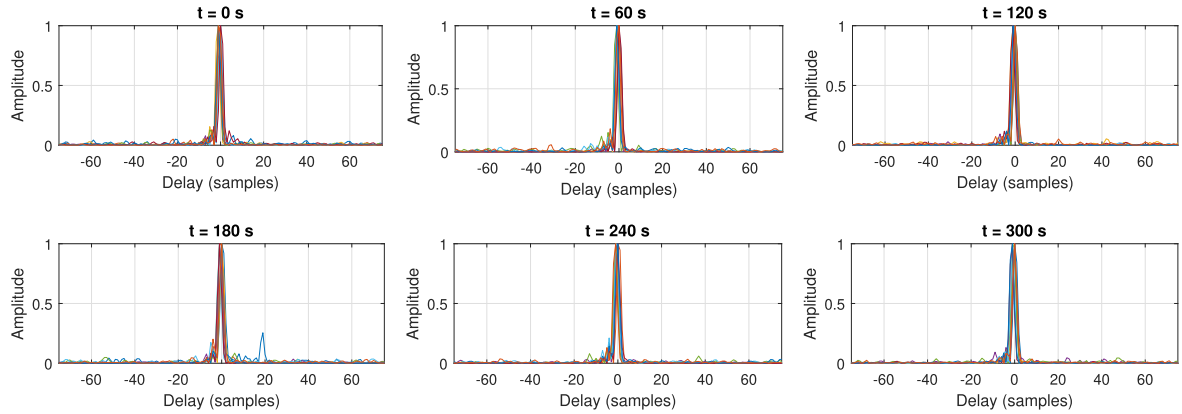

Fig. 5. Channel impulse response measured using the autocorrelation function of the CDMA shortcode for all 9 BTSs over 300 seconds in the environment near Riverside, California, USA.

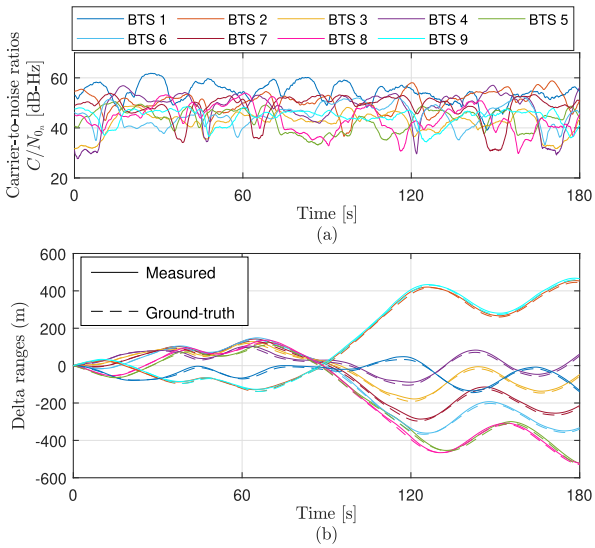

Fig. 6. (a) Carrier-to-noise ratios $\{C/N_{0_n}\}_{n=1}^{9}$ of all the cellular BTSs measured by the rover in the experiment. The carrier-to-noise ratios measured by the base were of similar values. (b) Measured and calculated delta ranges to all the cellular BTSs from the rover in the experiment. Similarly, the base's measured delta ranges closely matched the calculated delta ranges.

TABLE II
EXPERIMENTAL RESULTS ($k_\zeta T = 99$ s)

	$k < k_\zeta$	$k \geq k_\zeta$	$\forall k$
Duration	99 s	141 s	240 s
Distance traveled	0.68 km	1.56 km	2.24 km
Trajectory radius	175 m	282 m	270 m
EKF RMSE	22.11 m	4.05 m	14.53 m
B–WNLS RMSE	2.5 m	–	–
PS–WNLS RMSE	2.5 m	2.65 m	2.59 m
No Test RMSE	–	–	12.26 m

from Fig. 9(c) that $\Pr[\|\delta \boldsymbol{r}_{r_U}\|_2^2 \leq \zeta_2^2] = 0.88 \geq 1 - \alpha$, where α was chosen to be 0.4 for both experiments. This demonstrates that the proposed navigation strategy achieves the bounded-error requirement. For comparison, a navigation solution referred to as "No Test" trajectory was computed at the second time-step instead of determining k_ζ from the proposed test. The RMSE of

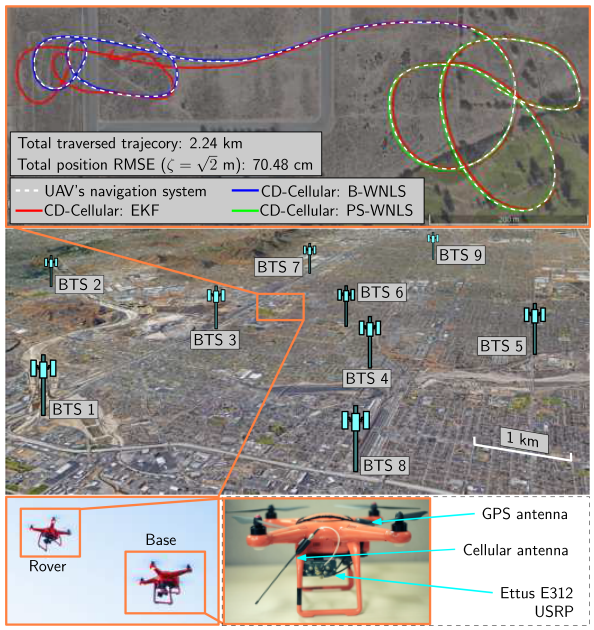

Fig. 7. Experimental setup, the cellular BTS layout, and the true trajectory (from the UAV's on-board integrated navigation system) and estimated trajectory (from the proposed CD-cellular framework for $\zeta = \sqrt{2}$ m) of the navigating UAV. The ground-truth trajectory is shown in white, the EKF trajectory estimate in red, the B-WNLS solution in blue, and the P-WNLS solution in green. The white curve coincides almost completely with the blue and green curves. Map data: Google Earth.

the No Test trajectory was found to be 12.26 m, which is also summarized in Table I and Table II.

It is important to note that the proposed CD-cellular framework is designed to guarantee a positioning performance under integer ambiguity errors only. However, when measurement noise dominates and in the presence of unmodeled errors (e.g., multipath), the effect the integer ambiguity errors may have on the positioning error becomes less significant. As a result, there is a fundamental lower bound on the position error that is a function of the unknown environment. This also implies that the proposed framework performs well in a practical regime of the design parameters α, β, ζ, and N. Nevertheless, the proposed method

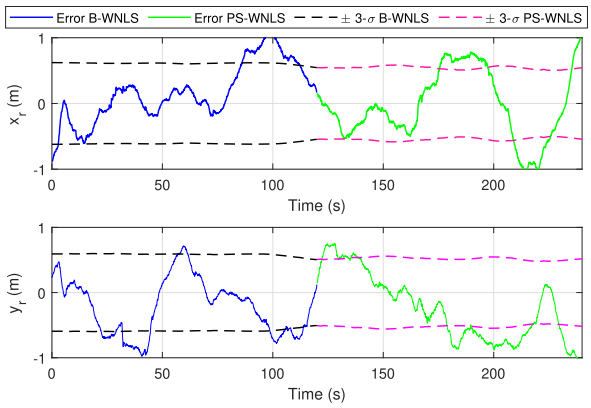

Fig. 8. Position error and associated ± 3-σ bounds for $\zeta = \sqrt{2}$ m.

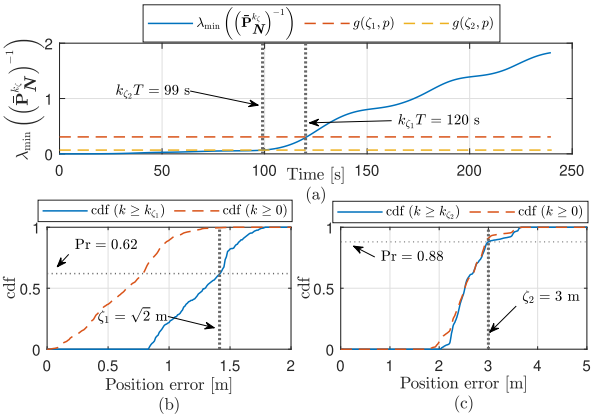

Fig. 9. (a) Time history of $\lambda_{\min}((\bar{\mathbf{P}}_{\boldsymbol{N}}^{k_\zeta})^{-1})$ and the thresholds $g(\zeta_1, p)$ and $g(\zeta_2, p)$. It can be seen that the tests are satisfied for $k_{\zeta_1} T = 120$ s and $k_{\zeta_2} T = 99$ s, respectively. (b) Cdf of the position error for $k \geq k_{\zeta_1}$ and $k \geq 0$, using the B-WNLS estimate for $k < k_{\zeta_1}$. It can be empirically seen that $\Pr\left[\left\|\delta \boldsymbol{r}_{r_U}\right\|_2^2 \leq \zeta_1^2\right] = 0.62 \geq 1 - \alpha$, where $\alpha = 0.4$. (c) Cdf of the position error for $k \geq k_{\zeta_2}$ and $k \geq 0$, using the B-WNLS estimate for $k < k_{\zeta_2}$. It can be empirically seen that $\Pr\left[\left\|\delta \boldsymbol{r}_{r_U}\right\|_2^2 \leq \zeta_2^2\right] = 0.88 \geq 1 - \alpha$, where $\alpha = 0.4$.

guarantees with a desired confidence level that the position error due to integer ambiguity errors remains below a desired threshold.

C. Discussion

The following are key takeaways and remarks from the experimental results presented above. First, it is important to note that the RMSEs were calculated with respect to the trajectory returned by the UAVs' on-board navigation system. Although these systems use multiple sensors for navigation, they are not equipped with high precision GPS receivers, e.g., RTK systems. Therefore, some errors are expected in what is considered to be "true" trajectories taken from the on-board sensors. The hovering horizontal precision of the UAVs are reported to be 2 m. It is worth noting that ideally, one would set the base to be stationary at an accurately surveyed position. However, considering the nature and limitations of the conducted experiment, the base was a hovering UAV. In such case, if the base's reported position from its GPS-INS system exhibited a bias, such bias would get consumed into the integer ambiguity term (cf. (7)), which is subsequently estimated. Note that the framework still achieved the desired performance on the rover UAV, despite the use of a non-stationary base UAV.

Second, the experiments showed that reliable navigation with cellular signals is possible when the proper models are used in an open semi-urban environment. The experiments lasted 4 minutes, indicating that the UAV could rely *exclusively* on cellular carrier phase measurements for sustained submeter-level accurate navigation. Note that the proposed framework does not account for unmodeled errors, such as multipath or signal blockage. Such errors could be partially mitigated (i) at the receiver level [24], [66], (ii) via outlier rejection techniques [57], [80], or (iii) included in the measurement model [59], [73], after which the proposed framework must be adapted. It is expected for the performance to degrade in the presence of such errors. Extending the proposed framework to account for such errors could be the subject of future work.

Third, not only the UAV can navigate at submeter-level accuracy in the absence of GPS signals, but it can do so with bounded errors. This is inherent to the formulation of the CD-cellular framework. Fig. 9(b) is clearly satisfying (11) for $\beta = 0.99$, $\alpha = 0.4$, and $\zeta = \sqrt{2}$ m.

Fourth, throughout the experiments, the UAV and base remained within the same BTS or eNB sectors. BTSs and eNBs typically transmit in three different sectors, each of which covering 120 degrees. When crossing between sectors, the receiver would need to perform a "handover," which involves acquiring and tracking the signal from the new sector [20]. The CD-cellular framework is robust against the BTS sectors not being completely synchronized when the UAV and the base are listening the same BTS sectors. However, errors in the measurements may be introduced when the UAV and base are in different sectors of a particular BTSs. One way to reduce the effect of the errors introduced by crossing BTS sectors is to use the approach proposed in [38].

Fifth, the distance between the base and rover varied from 272 m to 580 m throughout the experiment. The CD-cellular measurement model in (7) does not require a minimum or maximum separation between the base and navigating UAV. However, the maximum separation is dependent on the signal quality. It was shown in [44] that a cellular SOP receiver can acquire and track a BTS signal reliably up to a distance of 6 km. As such, the base and the UAV must each be within 6 km of a BTS to form differential measurement to that particular BTS. Several bases could be deployed to cover a larger area.

Sixth, in the CD-cellular framework formulation, the UAV-mounted receiver's clock bias is canceled by differencing measurements. As such, the magnitude of the receiver's clock bias should not affect the position estimate. This implies that the quality of the receiver's clock should not affect the navigation performance, as long as the receiver can maintain track of the signals.

Seventh, in order to assess the effect of altimeter errors on the 2–D navigation solution, a zero-mean, Gaussian measurement noise error was simulated in $\Delta z_{r,s_n}$ with a 100 m^2 variance. The 2–D position RMSE for all k for the experiment was 78.8 cm (increase of 8.32 cm) for $\zeta = \sqrt{2}$ m. The degradation in the 2–D navigation solution is up to two orders of magnitudes less than the altimeter errors.

Eighth, some of the position errors are due to vehicle dynamics, mainly during turns. The dynamic stress on the receiver's tracking loops will induce carrier phase measurements error, which in turn translate to position errors. The effects of dynamics can be seen by comparing Fig. 6 and Fig. 8. One can see that the error trend in Fig. 8 follows the variations due to turns in the delta range shown in Fig. 6. Higher order loops or vector tracking loops could be used in the cellular receiver to minimize the effects of dynamics on the measurements.

Ninth, while the experimental results presented herein are not extensive, they present solid evidence of the potential of the proposed approach. Beside the submeter-level RMSE achieved, it is evident from the $\pm 3-\sigma$ bounds shown in Fig. 8, which remain below 1 m in magnitude, that the position error is not expected to grow over time if the navigating UAV traveled a longer distance.

Tenth, it can be seen from Table I and Table II that not performing the proposed test results in a jump in the position RMSE. This indicates that a probabilistic bound can be guaranteed only when the proposed test is satisfied.

V. Conclusion

This paper presented a framework for submeter-accurate UAV horizontal navigation with cellular carrier phase measurements. The proposed framework, called CD-cellular framework, relies on a base receiver and a navigating receiver on-board a navigating UAV, also known as rover. Both receivers make carrier phase measurements to the same sectors of the same cellular SOPs to produce the cellular carrier phase double difference measurements, referred to as CD-cellular measurements. The main strategy behind the CD-cellular framework is to navigate in three stages. In the first stage, an EKF is employed to produce a coarse estimate of the UAV's position. In the second stage, which is determined by a proposed test on the estimation error covariance, the UAV fixes the integer ambiguities in a batch solver. The proposed test guarantees that the position error of the UAV will remain less than a pre-defined threshold with a desired probability after the batch solution is calculated. In the third stage, the UAV navigates with high precision with the CD-cellular measurements and fixed integer ambiguities. The proposed method is designed for environments with strong LOS signal. Further analysis should be conducted to extend the proposed approach to multipath environments. Experimental results demonstrated not only that the proposed framework guarantees a desired navigation performance, but it also showed a UAV navigating in an open semi-urban environment and multipath-free, LOS conditions with a 70.48 cm horizontal position RMSE over a trajectory of 2.24 km with reference to the UAV's navigation solution from its onboard GPS-INS system.

Appendix A
Proof That Only 2×2 Matrices Are Needed to be Inverted to Compute $(\bar{\mathbf{P}}_{\boldsymbol{N}}^{k_\zeta})^{-1}$

From (20) and (32), one can readily see that

$$\begin{aligned}\left(\bar{\mathbf{P}}_{\boldsymbol{N}}^{k_\zeta}\right)^{-1} &= \left[\lambda^2\mathbf{P}_{\boldsymbol{N}}^{k_\zeta}+\mathbf{R}_{\mathrm{U,B}}\right]^{\frac{1}{2}}\left(\mathbf{P}_{\boldsymbol{N}}^{k_\zeta}\right)^{-1}\left[\lambda^2\mathbf{P}_{\boldsymbol{N}}^{k_\zeta}+\mathbf{R}_{\mathrm{U,B}}\right]^{\frac{1}{2}}\\ &= \left[\lambda^2\mathbf{I}+\left(\mathbf{P}_{\boldsymbol{N}}^{k_\zeta}\right)^{-1}\mathbf{R}_{\mathrm{U,B}}\right]^{\frac{1}{2}}\left[\lambda^2\mathbf{I}+\mathbf{R}_{\mathrm{U,B}}\left(\mathbf{P}_{\boldsymbol{N}}^{k_\zeta}\right)^{-1}\right]^{\frac{1}{2}},\end{aligned}$$

which shows that the calculation of $(\bar{\mathbf{P}}_{\boldsymbol{N}}^{k_\zeta})^{-1}$ entails knowing $(\mathbf{P}_{\boldsymbol{N}}^{k_\zeta})^{-1}$. The estimation error covariance of the B-WNLS $\mathbf{P}_{\mathrm{B-WNLS}}^{k_\zeta}$ is given by

$$\mathbf{P}_{\mathrm{B-WNLS}}^{k_\zeta} = \left[\left(\tilde{\mathbf{H}}^{k_\zeta}\right)^{\mathsf{T}}\left(\mathbf{R}_{\mathrm{U,B}}^{k_\zeta}\right)^{-1}\tilde{\mathbf{H}}^{k_\zeta}\right]^{-1}, \tag{37}$$

where $\tilde{\mathbf{H}}^{k_\zeta} = [\tilde{\mathbf{G}}^{k_\zeta}\; \bar{\mathbf{I}}^{k_\zeta}]$, $\tilde{\mathbf{G}}^{k_\zeta} \triangleq \mathrm{diag}[\tilde{\mathbf{G}}(0),\ldots,\tilde{\mathbf{G}}(k_\zeta)]$. Note that $\tilde{\mathbf{G}}(k)$ is evaluated at the EKF position estimate at k. Expanding (37) and using matrix block inversion, $(\mathbf{P}_{\boldsymbol{N}}^{k_\zeta})^{-1}$ may be expressed as

$$\begin{aligned}\left(\mathbf{P}_{\boldsymbol{N}}^{k_\zeta}\right)^{-1} = \lambda^2\sum_{\kappa=0}^{k_\zeta}\Big[&\mathbf{R}_{\mathrm{U,B}}^{-1}(\kappa)-\mathbf{R}_{\mathrm{U,B}}^{-1}(\kappa)\tilde{\mathbf{G}}(\kappa)\\ &\cdot\left[\tilde{\mathbf{G}}^{\mathsf{T}}(\kappa)\mathbf{R}_{\mathrm{U,B}}^{-1}(\kappa)\tilde{\mathbf{G}}(\kappa)\right]^{-1}\tilde{\mathbf{G}}^{\mathsf{T}}(\kappa)\mathbf{R}_{\mathrm{U,B}}^{-1}(\kappa)\Big].\end{aligned} \tag{38}$$

The calculation of $\mathbf{R}_{\mathrm{U,B}}^{-1}(\kappa)$ is straightforward from the structure of $\mathbf{R}_{\mathrm{U,B}}(\kappa)$ in (10) and the Sherman-Morrison formula, which is given by

$$\begin{aligned}\mathbf{R}_{\mathrm{U,B}}^{-1}(\kappa) = &\left[\mathbf{R}^{(1)}(\kappa)\right]^{-1}\\ &-\frac{\left[\mathbf{R}^{(1)}(\kappa)\right]^{-1}\mathbf{1}_{N-1}\mathbf{1}_{N-1}^{\mathsf{T}}\left[\mathbf{R}^{(1)}(\kappa)\right]^{-1}}{\frac{1}{\left[\sigma_1^{(\mathrm{U,B})}(\kappa)\right]^2}+\mathbf{1}_{N-1}^{\mathsf{T}}\left[\mathbf{R}^{(1)}(\kappa)\right]^{-1}\mathbf{1}_{N-1}}.\end{aligned} \tag{39}$$

Recall that $\mathbf{R}^{(1)}(\kappa)$ is a diagonal matrix and its inverse can be trivially obtained. Consequently, calculating $(\mathbf{P}_{\boldsymbol{N}}^{k_\zeta})^{-1}$ and subsequently $(\bar{\mathbf{P}}_{\boldsymbol{N}}^{k_\zeta})^{-1}$ requires inverting only the matrices $\{\tilde{\mathbf{G}}^{\mathsf{T}}(\kappa)\mathbf{R}_{\mathrm{U,B}}^{-1}(\kappa)\tilde{\mathbf{G}}(\kappa)\}_{\kappa=0}^{k_\zeta}$, each of which is a 2×2 matrix.

Acknowledgment

The authors would like to thank Joshua Morales, Kimia Shamaei, and Mahdi Maaref for their help in data collection.

References

[1] T. Reid et al., "Localization requirements for autonomous vehicles," *SAE Int. J. Connected Automated Veh.*, vol. 2, no. 3, pp. 173–190, Sep. 2019.

[2] Federal Aviation Administration, "NextGen annual report: A report on the history, current status, and future of national airspace system modernization," pp. 1–154, 2020.

[3] R. Sabatini et al., "Avionics systems panel research and innovation perspectives," *IEEE Aerosp. Electron. Syst. Mag.*, vol. 35, no. 12, pp. 58–72, Dec. 2020.

[4] D. Borio, F. Dovis, H. Kuusniemi, and L. Presti, "Impact and detection of GNSS jammers on consumer grade satellite navigation receivers," *Proc. IEEE*, vol. 104, no. 6, pp. 1233–1245, Jun. 2016.

[5] R. Ioannides, T. Pany, and G. Gibbons, "Known vulnerabilities of global navigation satellite systems, status, and potential mitigation techniques," *Proc. IEEE*, vol. 104, no. 6, pp. 1174–1194, Jun. 2016.

[6] N. Kbayer and M. Sahmoudi, "Performances analysis of GNSS NLOS bias correction in urban environment using a threedimensional city model and GNSS simulator," *IEEE Trans. Aerosp. Electron. Syst.*, vol. 54, no. 4, pp. 1799–1814, Aug. 2018.

[7] D. Miralles et al. "An assessment of GPS spoofing detection via radio power and signal quality monitoring for aviation safety operations," *IEEE Intell. Transp. Syst. Mag.*, vol. 12, no. 3, pp. 136–146, Fall. 2020.

[8] D. Venable and J. Raquet, "Large scale image aided navigation," *IEEE Trans. Aerosp. Electron. Syst.*, vol. 52, no. 6, pp. 2849–2860, Dec. 2016.

[9] K. Takeyama, T. Machida, Y. Kojima, and N. Kubo, "Improvement of dead reckoning in urban areas through integration of low-cost multisensors," *IEEE Trans. Intell. Veh.*, vol. 2, no. 4, pp. 278–287, Dec. 2017.

[10] J. Zhang and S. Singh, "Visual-lidar odometry and mapping: Low-drift, robust, and fast," in *Proc. IEEE Int. Conf. Robot. Automat.*, 2015, pp. 2174–2181.

[11] J. Khalife, S. Ragothaman, and Z. Kassas, "Pose estimation with lidar odometry and cellular pseudoranges," in *Proc. IEEE Intell. Veh. Symp.*, 2017, pp. 1722–1727.

[12] L. Li, M. Yang, L. Guo, C. Wang, and B. Wang, "Hierarchical neighborhood based precise localization for intelligent vehicles in urban environments," *IEEE Trans. Intell. Veh.*, vol. 1, no. 3, pp. 220–229, Sep. 2016.

[13] Z. Wang, J. Fang, X. Dai, H. Zhang, and L. Vlacic, "Intelligent vehicle self-localization based on double-layer features and multilayer LIDAR," *IEEE Trans. Intell. Veh.*, vol. 5, no. 4, pp. 616–625, Dec. 2020.

[14] Y. Ren, B. Liu, R. Cheng, and C. Agia, "Lightweight semantic-aided localization with spinning LiDAR sensor," *IEEE Trans. Intell. Veh.*, to be published, doi: 10.1109/TIV.2021.3099022.

[15] T. Reid, A. Neish, T. Walter, and P. Enge, "Broadband LEO constellations for navigation," *Navigation: J. Inst. Navigation*, vol. 65, no. 2, pp. 205–220, 2018.

[16] Z. Kassas et al. "Enter LEO on the GNSS stage: Navigation with Starlink satellites," *Inside GNSS Mag.*, vol. 16, no. 6, pp. 42–51, 2021.

[17] C. Zhao, H. Qin, and Z. Li, "Doppler measurements from multiconstellations in opportunistic navigation," *IEEE Trans. Instrum. Meas.*, vol. 71, 2022, Art. no. 8500709.

[18] C. Yang, T. Nguyen, and E. Blasch, "Mobile positioning via fusion of mixed signals of opportunity," *IEEE Aerosp. Electron. Syst. Mag.*, vol. 29, no. 4, pp. 34–46, Apr. 2014.

[19] L. Chen, P. Thevenon, G. Seco-Granados, O. Julien, and H. Kuusniemi, "Analysis on the TOA tracking with DVB-T signals for positioning," *IEEE Trans. Broadcast.*, vol. 62, no. 4, pp. 957–961, Dec. 2016.

[20] J. Khalife, K. Shamaei, and Z. Kassas, "Navigation with cellular CDMA signals—Part I: Signal modeling and software-defined receiver design," *IEEE Trans. Signal Process.*, vol. 66, no. 8, pp. 2191–2203, Apr. 2018.

[21] C. Gentner, "Channel-SLAM: Multipath assisted positioning," Ph.D. dissertation, Ulm University, Ulm, Germany, 2018.

[22] J. del Peral-Rosado, R. Raulefs, J. López-Salcedo, and G. Seco-Granados, "Survey of cellular mobile radio localization methods: From 1G to 5G," *IEEE Commun. Surv. Tuts.*, vol. 20, no. 2, pp. 1124–1148, Apr.–Jul. 2018.

[23] T. Kang, H. Lee, and J. Seo, "TOA-based ranging method using CRS in LTE signals," *J. Adv. Navigation Technol.*, vol. 23, no. 5, pp. 437–443, Oct. 2019.

[24] P. Wang and Y. Morton, "Multipath estimating delay lock loop for LTE signal TOA estimation in indoor and urban environments," *IEEE Trans. Wireless Commun.*, vol. 19, no. 8, pp. 5518–5530, Aug. 2020.

[25] J. Gante, L. Sousa, and G. Falcao, "Dethroning GPS: Low-power accurate 5G positioning systems using machine learning," *IEEE Trans. Emerg. Sel. Topics Circuits Syst.*, vol. 10, no. 2, pp. 240–252, Jun. 2020.

[26] A. Abdallah and Z. Kassas, "UAV navigation with 5G carrier phase measurements," in *Proc. ION GNSS Conf.*, 2021, pp. 3294–3306.

[27] C. Gentner, T. Jost, W. Wang, S. Zhang, A. Dammann, and U. Fiebig, "Multipath assisted positioning with simultaneous localization and mapping," *IEEE Trans. Wireless Commun.*, vol. 15, no. 9, pp. 6104–6117, Sep. 2016.

[28] J. del Peral-Rosado, J. López-Salcedo, F. Zanier, and G. Seco-Granados, "Position accuracy of joint time-delay and channel estimators in LTE networks," *IEEE Access*, vol. 6, pp. 25185–25199, 2018.

[29] Z. Kassas, M. Maaref, J. Morales, J. Khalife, and K. Shamaei, "Robust vehicular localization and map matching in urban environments through IMU, GNSS, and cellular signals," *IEEE Intell. Transp. Syst. Mag.*, vol. 12, no. 3, pp. 36–52, Fall 2020.

[30] R. Landry, A. Nguyen, H. Rasaee, A. Amrhar, X. Fang, and H. Benzerrouk, "Iridium Next LEO satellites as an alternative PNT in GNSS denied environments–part 1," *Inside GNSS Mag.*, vol. 14, no. 3, pp. 56–64, May 2019.

[31] J. Khalife and Z. Kassas, "Opportunistic UAV navigation with carrier phase measurements from asynchronous cellular signals," *IEEE Trans. Aerosp. Electron. Syst.*, vol. 56, no. 4, pp. 3285–3301, Aug. 2020.

[32] C. Yang and A. Soloviev, "Mobile positioning with signals of opportunity in urban and urban canyon environments," in *Proc. IEEE/ION Position, Location, Navigation Symp.*, 2020, pp. 1043–1059.

[33] N. Souli, P. Kolios, and G. Ellinas, "Online relative positioning of autonomous vehicles using signals of opportunity," *IEEE Trans. Intell. Veh.*, to be published, doi: 10.1109/TIV.2021.3124727.

[34] M. Lichtman, R. Rao, V. Marojevic, J. Reed, and R. Jover, "5G NR jamming, spoofing, and sniffing: Threat assessment and mitigation," in *Proc. IEEE Int. Conf. Commun. Workshops*, 2018, pp. 1–6.

[35] A. Gupta, R. Jha, P. Gandotra, and S. Jain, "Bandwidth spoofing and intrusion detection system for multistage 5G wireless communication network," *IEEE Trans. Veh. Technol.*, vol. 67, no. 1, pp. 618–632, Jan. 2018.

[36] W. Xu, C. Yuan, S. Xu, H. Ngo, and W. Xiang, "On pilot spoofing attack in massive MIMO systems: Detection and countermeasure," *IEEE Trans. Inf. Forensics Secur.*, vol. 16, pp. 1396–1409, 2021.

[37] A. Abdallah, J. Khalife, and Z. Kassas, "Experimental characterization of received 5G signals carrier-to-noise ratio in indoor and urban environments," in *Proc. IEEE Veh. Technol. Conf.*, 2021, pp. 1–5.

[38] J. Khalife and Z. Kassas, "Navigation with cellular CDMA signals—Part II: Performance analysis and experimental results," *IEEE Trans. Signal Process.*, vol. 66, no. 8, pp. 2204–2218, Apr. 2018.

[39] C. Yang and A. Soloviev, "Simultaneous localization and mapping of emitting radio sources-SLAMERS," in *Proc. ION GNSS Conf.*, 2015, pp. 2343–2354.

[40] J. Morales and Z. Kassas, "Tightly-coupled inertial navigation system with signals of opportunity aiding," *IEEE Trans. Aerosp. Electron. Syst.*, vol. 57, no. 3, pp. 1930–1948, Jun. 2021.

[41] P. Misra and P. Enge, *Global Positioning System: Signals, Measurements, and Performance*, 2nd ed., Lincoln, MA, USA: Ganga-Jamuna Press, 2010.

[42] D. Yoon, C. Kee, J. Seo, and B. Park, "Position accuracy improvement by implementing the DGNSS-CP algorithm in smartphones," *Sensors*, vol. 16, no. 6, pp. 910–925, 2016.

[43] J. Khalife and Z. Kassas, "Precise UAV navigation with cellular carrier phase measurements," in *Proc. IEEE/ION Position, Location, Navigation Symp.*, 2018, pp. 978–989.

[44] J. Khalife, K. Shamaei, S. Bhattacharya, and Z. Kassas, "Centimeter-accurate UAV navigation with cellular signals," in *Proc. ION GNSS Conf.*, 2018, pp. 2321–2331.

[45] P. Teunissen and S. Verhagen, "GNSS carrier phase ambiguity resolution: Challenges and open problems," in *Observing our Changing Earth*. Berlin/Heidelberg, Germany: Springer, 2009, pp. 785–792.

[46] K. Berntorp, A. Weiss, and S. Cairano, "Integer ambiguity resolution by mixture Kalman filter for improved GNSS precision," *IEEE Trans. Aerosp. Electron. Syst.*, vol. 56, no. 4, pp. 3170–3181, Aug. 2020.

[47] M. Pratt, B. Burke, and P. Misra, "Single-epoch integer ambiguity resolution with GPS-GLONASS L1 data," in *Proc. Annu. Meeting The Inst. Navigation*, 1997, pp. 691–699.

[48] P. Teunissen, "Least-squares estimation of the integer GPS ambiguities," in *Proc. Invited Lecture, Sect. IV Theory And Methodol., IAG Gen. Meeting*, 1993, pp. 1–16.

[49] P. Teunissen, "The least-squares ambiguity decorrelation adjustment: A method for fast GPS integer ambiguity estimation," *J. Geodesy*, vol. 70, no. 1, pp. 65–82, Nov. 1995.

[50] P. Teunissen, "Carrier phase integer ambiguity resolution," in *Springer Handbook of Global Navigation Satellite Systems*, New York, NY, USA: Springer, 2017, pp. 661–685.

[51] X. Chang, X. Yang, and T. Zhou, "MLAMBDA: A modified LAMBDA method for integer least-squares estimation," *J. Geodesy*, vol. 79, no. 9, pp. 552–565, 2005.

[52] B. Pervan and B. Parkinson, "Cycle ambiguity estimation for aircraft precision landing using the Global Positioning System," *J. Guidance, Control, Dyn.*, vol. 20, no. 4, pp. 681–689, Jul./Aug. 1997.
[53] J. del Peral-Rosado et al., "Software-defined radio LTE positioning receiver towards future hybrid localization systems," in *Proc. AIAA Int. Commun. Satell. Syst. Conf.*, 2013, pp. 1–11.
[54] M. Ulmschneider and C. Gentner, "Multipath assisted positioning for pedestrians using LTE signals," in *Proc. IEEE/ION Position, Location, Navigation Symp.*, 2016, pp. 386–392.
[55] M. Driusso, C. Marshall, M. Sabathy, F. Knutti, H. Mathis, and F. Babich, "Vehicular position tracking using LTE signals," *IEEE Trans. Veh. Technol.*, vol. 66, no. 4, pp. 3376–3391, Apr. 2017.
[56] A. Abdallah and Z. Kassas, "Multipath mitigation via synthetic aperture beamforming for indoor and deep urban navigation," *IEEE Trans. Veh. Technol.*, vol. 70, no. 9, pp. 8838–8853, Sep. 2021.
[57] M. Maaref and Z. Kassas, "Measurement characterization and autonomous outlier detection and exclusion for ground vehicle navigation with cellular signals," *IEEE Trans. Intell. Veh.*, vol. 5, no. 4, pp. 670–683, Dec. 2020.
[58] S. Ragothaman, M. Maaref, and Z. Kassas, "Autonomous ground vehicle path planning in urban environments using GNSS and cellular signals reliability maps: Models and algorithms," *IEEE Trans. Aerosp. Electron. Syst.*, vol. 57, no. 2, pp. 1562–1580, Jun. 2021.
[59] M. Maaref, J. Khalife, and Z. Kassas, "Aerial vehicle protection level reduction by fusing GNSS and terrestrial signals of opportunity," *IEEE Trans. Intell. Transp. Syst.*, vol. 22, no. 9, pp. 5976–5993, Sep. 2021.
[60] Qualcomm Technologies, Inc., "LTE unmanned aircraft systems," Tech. Rep. 1.0.1, May 2017. [Online]. Available: https://www.qualcomm.com/documents/lte-unmanned-aircraft-systems-trial-report/
[61] Z. Kassas et al., "Assessment of cellular signals of opportunity for high altitude aircraft navigation," *IEEE Aerospace and Electronic Systems Magazine*, to be published, doi: 10.1109/MAES.2022.3187142.
[62] X. Chen, F. Dovis, and M. Pini, "An innovative multipath mitigation method using coupled amplitude delay lock loops in GNSS receivers," in *Proc. IEEE/ION Position, Location Navigation Symp.*, 2010, pp. 1118–1126.
[63] K. Shamaei and Z. Kassas, "LTE receiver design and multipath analysis for navigation in urban environments," *Navigation: J. Inst. Navigation*, vol. 65, no. 4, pp. 655–675, Dec. 2018.
[64] Y. Quan, L. Lau, G. Roberts, X. Meng, and C. Zhang, "Convolutional neural network based multipath detection method for static and kinematic GPS high precision positioning," *Remote Sens.*, vol. 10, no. 12, pp. 2052–2069, Dec. 2018.
[65] P. Gadka, J. Sadowski, and J. Stefanski, "Detection of the first component of the received LTE signal in the OTDoA method," *Wireless Commun. Mobile Comput.*, 2019, pp. 1–12, Apr. 2019.
[66] H. Dun, C. Tiberius, and G. Janssen, "Positioning in a multipath channel using OFDM signals with carrier phase tracking," *IEEE Access*, vol. 8, pp. 13011–13028, 2020.
[67] P. Wang, Y. Wang, and J. Morton, "Signal tracking algorithm with adaptive multipath mitigation and experimental results for LTE positioning receivers in urban environments," *IEEE Trans. Aerosp. Electron. Syst.*, vol. 58, no. 4, pp. 2779–2795, Aug. 2022.
[68] M. Joerger and B. Pervan, "Fault detection and exclusion using solution separation and chi-squared ARAIM," *IEEE Trans. Aerosp. Electron. Syst.*, vol. 52, no. 2, pp. 726–742, Apr. 2016.
[69] N. Zhu, J. Marais, D. Betaille, and M. Berbineau, "GNSS position integrity in urban environments: A. review of literature," *IEEE Trans. Intell. Transp. Syst.*, vol. 19, no. 9, pp. 2762–2778, Sep. 2018.
[70] N. Zhu, D. Betaille, J. Marais, and M. Berbineau, "GNSS integrity monitoring schemes for terrestrial applications in harsh signal environments," *IEEE Intell. Transp. Syst. Mag.*, vol. 12, no. 3, pp. 81–91, Fall 2020.
[71] M. Jia, H. Lee, J. Khalife, Z. Kassas, and J. Seo, "Ground vehicle navigation integrity monitoring for multi-constellation GNSS fused with cellular signals of opportunity," in *Proc. IEEE Int. Conf. Intell. Transp. Syst.*, 2021, pp. 3978–3983.
[72] N. Ziedan, "Multipath channel estimation and pattern recognition for environment-based adaptive tracking," in *Proc. 25th Int. Tech. Meeting Satell. Division Inst. Navigation*, 2012, pp. 394–407.
[73] Y. Wang, X. Chen, and P. Liu, "Statistical multipath model based on experimental GNSS data in static urban canyon environment," *Sensors*, vol. 18, no. 4, pp. 1149–1165, Apr. 2018.
[74] Y. Bar-Shalom, X. Li, and T. Kirubarajan, *Estimation with Applications to Tracking and Navigation*. New York, NY: Wiley, 2002.
[75] B. Noble and J. Daniel, *Applied Linear Algebra*. Upper Saddle River, NJ, USA: Prentice Hall, 1998.
[76] M. Haenggi, J. Andrews, F. Baccelli, O. Dousse, and M. Franceschetti, "Stochastic geometry and random graphs for the analysis and design of wireless networks," *IEEE J. Sel. Areas Commun.*, vol. 27, no. 7, pp. 1029–1046, Sep. 2009.
[77] J. Schloemann, H. Dhillon, and R. Buehrer, "A tractable metric for evaluating base station geometries in cellular network localization," *IEEE Wireless Commun. Lett.*, vol. 5, no. 2, pp. 140–143, Apr. 2016.
[78] J. Morales and Z. Kassas, "Optimal collaborative mapping of terrestrial transmitters: Receiver placement and performance characterization," *IEEE Trans. Aerosp. Electron. Syst.*, vol. 54, no. 2, pp. 992–1007, Apr. 2018.
[79] J. Wirth, E. Bonugli, and M. Freund, "Assessment of the accuracy of google earth imagery for use as a tool in accident reconstruction," in *Proc. SAE World Congr. & Exhib.*, 2015, pp. 1–17.
[80] M. Maaref and Z. Kassas, "Autonomous integrity monitoring for vehicular navigation with cellular signals of opportunity and an IMU," *IEEE Trans. Intell. Transp. Syst.*, vol. 23, no. 6, pp. 5586–5601, Jun. 2022.

Joe Khalife (Senior Member, IEEE) received the B.E. degree in electrical engineering and the M.S. degree in computer engineering from Lebanese American University (LAU), Beirut, Lebanon, and the Ph.D. degree in electrical engineering and computer science from the University of California Irvine, Irvine, CA, USA. He is currently a Postdoctoral Fellow with the University of California Irvine, and a Member of the Autonomous Systems Perception, Intelligence, and Navigation (ASPIN) Laboratory. From 2012 to 2015, he was a Research Assistant at LAU and has been a Member of the ASPIN Laboratory since 2015. His research interests include opportunistic navigation, autonomous vehicles, and software-defined radio. He was the recipient of the 2016 IEEE/ION Position, Location, and Navigation Symposium (PLANS) Best Student Paper Award and the 2018 IEEE Walter Fried Award.

Zaher (Zak) M. Kassas (Senior Member, IEEE) received the B.E. degree in electrical engineering from the Lebanese American University, Beirut, Lebanon, the M.S. degree in electrical and computer engineering from The Ohio State University, Columbus, OH, USA, the M.S.E. degree in aerospace engineering and the Ph.D. in electrical and computer engineering from The University of Texas at Austin, Austin, TX, USA. He is currently a Professor of electrical and computer engineering at The Ohio State University and Director of the Autonomous Systems Perception, Intelligence, and Navigation (ASPIN) Laboratory. He is also the Director of the U.S. Department of Transportation Center: CARMEN (Center for Automated Vehicle Research with Multimodal AssurEd Navigation), focusing on navigation resiliency and security of highly automated transportation systems. His research interests include cyber-physical systems, estimation theory, navigation systems, autonomous vehicles, and intelligent transportation systems. He was the recipient of the 2018 National Science Foundation (NSF) Faculty Early Career Development Program (CAREER) Award, 2019 Office of Naval Research (ONR) Young Investigator Program (YIP) Award, 2022 Air Force Office of Scientific Research (AFOSR) YIP Award, 2018 IEEE Walter Fried Award, 2018 Institute of Navigation (ION) Samuel Burka Award, and 2019 ION Col. Thomas Thurlow Award. He is a Senior Editor of the IEEE TRANSACTIONS ON INTELLIGENT VEHICLES and an Associate Editor for the IEEE TRANSACTIONS ON AEROSPACE AND ELECTRONIC SYSTEMS and IEEE TRANSACTIONS ON INTELLIGENT TRANSPORTATION SYSTEMS.